Study and Development of an Interrogation System for Fabry Perot Cavity Sensors

João Manuel Gonçalves Pereira dos Reis
Mestrado Integrado em Engenharia Física
Departamento de Física e Astronomia
2022

Orientador
Orlando José dos Reis Frazão, Investigador, INESCTEC

Coorientadora
Susana Oliveira Silva, Investigadora, INESCTEC

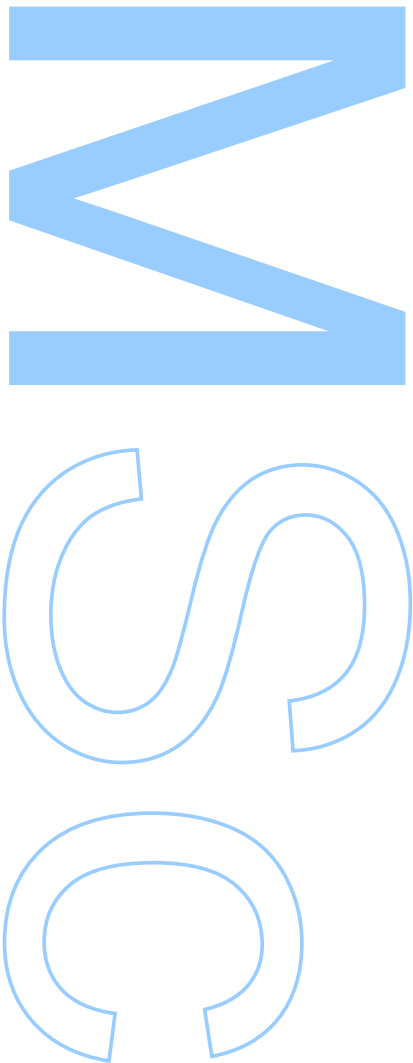

U.PORTO

FACULDADE DE CIÊNCIAS
UNIVERSIDADE DO PORTO

Todas as correções determinadas pelo júri, e só essas, foram efetuadas.

O Presidente do Júri,

Porto, _____/_____/_____

UNIVERSIDADE DO PORTO

MASTERS THESIS

Study and Development of an Interrogation System for Fabry Perot Cavity Sensors

Author:
João REIS

Supervisor:
Orlando FRAZÃO

Co-supervisor:
Susana SILVA

A thesis submitted in fulfilment of the requirements
for the degree of MSc. Engineering Physics

at the

Faculdade de Ciências da Universidade do Porto
Departamento de Física e Astronomia

December 9, 2022

“ All we have to decide is what to do with the time that is given us. ”

John Ronald Reuel Tolkien, in Fellowship of the Ring

Declaração de Honra

Eu, João Manuel Gonçalves Pereira dos Reis, inscrito no Mestrado em Engenharia Física da Faculdade de Ciências da Universidade do Porto declaro, nos termos do disposto na alínea a) do artigo 14.º do Código Ético de Conduta Académica da U.Porto, que o conteúdo da presente dissertação reflete as perspetivas, o trabalho de investigação e as minhas interpretações no momento da sua entrega. Ao entregar esta dissertação, declaro, ainda, que a mesma é resultado do meu próprio trabalho de investigação e contém contributos que não foram utilizados previamente noutros trabalhos apresentados a esta ou outra instituição. Mais declaro que todas as referências a outros autores respeitam escrupulosamente as regras da atribuição, encontrando-se devidamente citadas no corpo do texto e identificadas na secção de referências bibliográficas. Não são divulgados na presente dissertação quaisquer conteúdos cuja reprodução esteja vedada por direitos de autor. Tenho consciência de que a prática de plágio e auto-plágio constitui um ilícito académico.

João Manuel Gonçalves Pereira dos Reis

Porto, 03 de Outubro de 2022

Acknowledgements

First and foremost, I would like to thank both my parents and my sister for the unconditional love and support that they showed me throughout my whole life. They always proved to be a source of strength and were able to help me overcome the struggles I faced during my college years. Furthermore, I am certain that they will remain as my biggest pillars in all my future endeavours.

Secondly, I am thankful to my thesis advisor, Professor Orlando Frazão, for giving me the opportunity to work with him in my third year of college, and thus introducing me to the academic investigation world. I am also thankful for the fun and interesting stories which had the capacity of soothing the nerves. With him I learned immensely. Furthermore, I am also thankful to my co-supervisor Susana Silva for the support given during this last year.

On that note, I also would like to mention all the members of CAP, since from the beggining they were all very friendly. I would like to especially mention António Vaz Rodrigues and Paulo Robalinho. I will be always in gratitude to António for all the help during the long hours in the lab and the lengthy conversations about the most varied topics which helped to pass the time. To Paulo, I want to acknowledge the support given during the course of this dissertation, which was vital to better understand the theory behind the work.

I would also like to acknowledge ESA - European Space Agency which funded a part of my thesis work through the LIRA Project in accordance with the terms of ESA Contract No. 4000135481/21/NL/AR.

I also have to express my sincerest gratitude to PhysikUP as in my time spent there I was able to find a second home. I will always treasure PhysikUP as through it I made some very good friends. At the same time I also grew as a person and left PhysikUP as a better version of myself. To Ana Carolina Silva, Ana Rita Bugalhão and Duarte Silva, I know I can be a handfull and was a little annoying at times. But in all honesty, you would not like me in any other way.

Speaking of friends, I also have to mention Ana Luísa (you will always be my *Pequenina*), Ana Carolina and Miguel Tomé. Since the 10^{th} grade that our friend group exists. And throughout all these years, the friendship never wavered. They were always there for me and I cherish the histories we have. The promise for a trip to Korea is written here!

Lastly, I want to apologize if I forgot to acknowledge someone and say that everyone who was in anyway present in my life made a contribute to the man I am today.

UNIVERSIDADE DO PORTO

Abstract

Faculdade de Ciências da Universidade do Porto
Departamento de Física e Astronomia

MSc. Engineering Physics

Study and Development of an Interrogation System for Fabry Perot Cavity Sensors

by João REIS

The work developed in the ambit of this dissertation is based on the use of optical fibre interferometers, namely Fabry Perot (FP) cavities and an interrogation system. Two different topics were explored in the present work.

The first part consisted on the fabrication of FP cavities with different lengths using a cost effective and easy to use method. The length of the produced FP cavities was in the range $[30, 1200]$ μm. After the fabrication, all the cavities were subjected to external parameters such as strain and temperature. The wavelength shift induced by the variation of external parameters was monitored via a Optical Spectrum Analyser (OSA) and the sensitivity of the sensors was determined. Finally, the influence of the sensor's length on the sensor sensitivity was examined. It was discovered that the sensitivity to strain varied with the FP cavity length while the sensitivity to temperature was found to be invariant.

The second part consisted in the development of an optical interrogation system capable of monitoring with higher resolution the response of a sensor induced by the variation of external parameters. The interrogation system consisted of a FP cavity attached to a Piezoelectric stack (PZT). By means of a photodetector, the optical signal was converted to an optoeletronic signal which was then displayed on an oscilloscope. After the development of the interrogation system and assuring its functioning, it was characterized to best understand its limitations. Finally, the interrogation system was used to monitor the optical length change of the FP sensor as external parameters were applied to it. Strain was induced in the FP sensor and a sensitivity of (-8.82 ± 0.12) $\mu s/\mu\epsilon$ $\mu s/\mu\epsilon$ was estimated. Moreover, the equilibrium length of the FP interrogator was decreased by means of a micro-translation stage and a sensitivity of (-5.84 ± 0.52) ms/μm was reported.

This work is inserted in the LIRA project supported by ESA whose goal is to deploy the developed prototype interrogation system on a satellite to monitor temperature variations of the order of μK.

UNIVERSIDADE DO PORTO

Resumo

Faculdade de Ciências da Universidade do Porto
Departamento de Física e Astronomia

Mestrado Integrado em Engenharia Física

Estudo e Desenvolvimento de um Sistema de Interrogação Ótica para Cavidades Sensoras Fabry Perot

por João REIS

O trabalho desenvolvido no âmbito desta dissertação lidou maioritariamente com o uso de interferómetros em fibra ótica, mais concretamente cavidades Fabry Perot (FP) e um sistema de interrogação ótico. Dois tópicos diferentes foram explorados no trabalho executado.

O trabalho inicial consistiu na fabricação de cavidades FP com diferentes comprimentos usando um método intuitivo e prático. As cavidades FP fabricadas têm comprimentos entre 30 e 1200 μm. Após o fábrico, todas as cavidades foram expostas a parâmetros externos como tensão e temperatura. O espetro ótico do sensor foi monitorizado com recurso a um Analisador de Espectros Óticos e a sensibilidade dos sensores foi estimada. Foi concluído que a sensibilidade à tensão varia com o comprimento da cavidade FP. Por outro lado concluiu-se que a sensibilidade à temperatura é invariante.

Posteriormente, o trabalho consistiu no desenvolvimento de um sistema de interrogação ótico capaz de monitorizar com maior resolução a resposta de um sensor FP induzida por parâmetros externos. O sistema de interrogação é composto por uma cavidade FP acoplada a um atuador piezoelétrico. O sinal ótico foi convertido num sinal optoeletrónico que posteriormente foi reproduzido num osciloscópio. Após o desenvolvimento do sistema de interrogação ótico e comprovar o seu funcionamento, o mesmo foi caracterizado para melhor entender as suas limitações.

Por fim, o sensor FP foi exposto a parâmetros externos e o sistema de interrogação foi usado para monitorizar o sinal optoeletrónico. Foi induzida tensão no sensor FP e a sensibilidade estimada foi de (-8.82 ± 0.12) μs/$\mu\epsilon$ $\mu s/\mu\epsilon$. Adicionalmente, com recurso

a um parafuso micrométrico o comprimento da cavidade FP interrogadora foi alterado e uma sensitividade de (-5.84 ± 0.52) ms$/\mu m$ foi reportada.

Este trabalho está inserido no projeto LIRA financiado pela ESA cujo objetivo é colocar o sistema de interrogação ótico desenvolvido num satélite para monitorizar variações de temperatura da ordem dos μK.

Contents

List of Figures

List of Tables

Abbreviations

FOS	Fibre Optical Sensors
FP	Fabry Perot
FFPI	Fibre Fabry Perot Interferometer
SMF	Single Mode Fibre
HCF	Hollow Core Fibre
FPI	Fabry Perot Interferometer
FSL	Fibre Sagnac Loops
FSR	Free Spectral Range
PZT	Piezoelectric stack
PCF	Photonic Cristal Fibre
FBG	Fibre Bragg Grating
EFPI	Extrinsic Fabry Perot Interferometer
RIU	Refractive Index Unit
OSA	Optical Spectrum Analyser

Chapter 1

Introduction

1.1 Motivation

There has always been a need to comprehend the world and gauge its physical characteristics. With the advent of electromagnetism in the end of the eighteenth century and early nineteenth century, the opportunity for using electronic sensors in sensing applications arose. However, despite the usefullness of this type of sensors they also have a few limitations such as susceptibility to electromagnetic interference, high weight and size, need for shielding [1], low biocompatibility [2], long term instability, excessive drift and fragility [3]. But with the development and optimization of the optical fibre in the late twentieth century [4] the idea of optical sensors emerged. Soon this type of sensors proved more useful than conventional sensors, due to the fact that these type of sensors are passive, have low attenuation and wide bandwidth [5]. Additionally, they also present the ability of optical and electrical multiplexing and are capable of widthstanding extreme temperatures [1]. Furthermore, Fibre Optical Sensors (FOS) are immune to electromagnetic interference [1], are used as distributed sensing [6] and can also be operated remotely [5].

A very common type of FOS is the low-finesse Fabry Perot Interferometer (FPI). This type of sensor shares the same advantages of FOS and also exhibits the advantages of simplicity, resistance to harsh environment and responsiveness [7]. This sensor can be employed in monitorization of several physical quantities, namely temperature [8–11], humidity [9], curvature [12], gas pressure [10, 13], strain [14], magnetic field [14] and biological sensing [3]. It also finds application in the field of civil engineering, where it is used in the context of structural monitoring [15]. Nonetheless, the full behaviour of Fabry

Perot (FP) sensors is still unknown, which in turn leads to the opportunity to characterize varied FP sensors with regards to physical parameters.

Furthermore, to be able to measure variations of the optical response induced by the physical quantity of interest, an optical interrogator is required. Traditionally, the optical interrogators used are Optical Spectrum Analysers (OSA). Nevertheless, because of its drawbacks such as low sweep speed [16], cost, volume and weight [17], as well as vulnerability to power fluctuations of broadband light sources [18] it is not suitable for use *in situ*, *i.e.*, outside of an academic environment. Therefore, a prototype optical interrogation system is in demand nowadays [19–22].

1.2 Objectives

The main goal was to investigate the relation between the length of FP cavities and the sensitivity to physical parameters such as strain and temperature. The objectives, then, are as follows:

- Manufacturing of in-fibre FPI with lengths in the range $[30, 1200]$ μm.
- Characterization in strain and temperature of all produced FPI.
- Determination of the relation between physical parameters sensitivity and the length of FPI.

Afterwards, the focus of this thesis turns to the development of a prototype optical interrogation system. During this work, the following goals are expected to be fullfilled:

- Manufacturing of an in-fibre FP cavity to simulate a sensor.
- Development of an optical interrogation system which consists of a in-air FP cavity attached to a Piezoelectric stack.
- Interrogation of the simulated sensor by the prototype optical interrogation system.
- Characterization in amplitude and frequency of the optic and optoeletronic signal of the system using a triangular applied electric signal.

1.3 Outline

This dissertation is divided in six chapters. The first three chapters present a brief overview of the theory and previous work done in the fields of optical sensors and interrogation systems. The remaining chapters describe the experimental work.

In the first chapter the motivation for the work developed in the course of this dissertation is presented whilst referencing the main objectives of this dissertation and enumerating the main publications that are based on the work that was carried out.

In the second chapter the importance of FOS and especially FP sensors is emphasised, as several research articles which analise the use of a FPI in a sensing configuration are discussed and the major findings reported. Furthermore, a brief review of the state of the art of prototype optical interrogation systems is also presented. Novel methods capable of demodulating with high speed and resolution the length of the interferometer and thus surpassing the traditional OSA are reported.

The third chapter serves as a support for the following two chapters as the fundamental theory needed to understand the behaviour of FPI and optical interrogation systems is explained. The main equations are presented and the simulations of these equations are displayed in graphical form and discussed.

In the fourth chapter the initial work done in the scope of this thesis is thoroughly reported. Firstly, the fabrication process of FP cavities is discussed. Afterwards, a study envolving the cavities, which had the goal of verifying the effect of the cavities length on the sensitivity to strain and temperature, is described.

The fifth chapter consists of the final work developed during this dissertation. The scheme of the optical interrogation system is introduced and explained. Thereafter, the main results of the characterization of the interrogation system are debated.

In the sixth and final chapter in a way of conclusion the major findings of the work executed throughout this dissertation are reported. Prospects of future work are also debated.

1.4 Outputs

Scientific journals

1. A. V. Rodrigues, **J. Reis**, A. J. M. Martins, C. S. Monteiro, S. O. Silva, C. M. R. Caridade, S. O. Tavares, and O. Frazão, "Cavity length dependence on strain sensitivity for Fabry–Perot sensors", *Microwave and Optical Technology Letters*, 2022, DOI: 10.1002/mop.33405

Communications in International Conferences

1. **J. Reis**, A. V. Rodrigues, P. Robalinho, S. Novais, J. Maia, P. Marques, D. Roma, J. Salvans, M. Canal, J. Ramos, V. Gualani, S. Sisteré, V. Martín, M. Nofrarias, S. Silva, and O. Frazão, "*White light interferometer for Fabry-Perot cavities sensors with absolute physical measurement* ", AOP 2022 - V International Conference on Applications of Optics and Photonics, Guimarães, Portugal, 2022

2. **J. Reis**, A. V. Rodrigues, P. Robalinho, S. Novais, J. Maia, P. Marques, D. Roma, J. Salvans, M. Canal, J. Ramos, V. Gualani, S. Sisteré, V. Martín, M. Nofrarias, S. Silva, and O. Frazão, "*The effect of frequency modulation on the FSR of a Fabry-Perot cavity using an Optical Spectrum Analyser*", EOSAM 2022 - European Optical Society Meeting, Porto, Portugal 2022

Chapter 2

State of the art

2.1 Fabry Perot Sensors

Optical sensing is now a widely used technology in several fields such as civil and geotechnical engineering [23], healthcare [24], navy [25] and oil and gas industry [26]. Several configurations of interferometers such as Mach-Zender, Michelson or Sagnac were already existent in 1982 [27]. Additionally, one of the most adaptable, straightforward, and widely used interferometers today is the Fabry Perot (FP) sensor.

The first in-fibre Fabry Perot Interferometer (FPI) was reported in 1982 by making use of a single mode fibre (SMF) with a 4 μm diameter silica core, a 125 μm diameter silica cladding and a 0.9 mm outer diameter nylon jacket [27]. In this paper, Yoshino *et al.* fabricated a FPI by coating the polished end faces of a SMF with a high reflectance dielectric using the vacuum evaporation method.

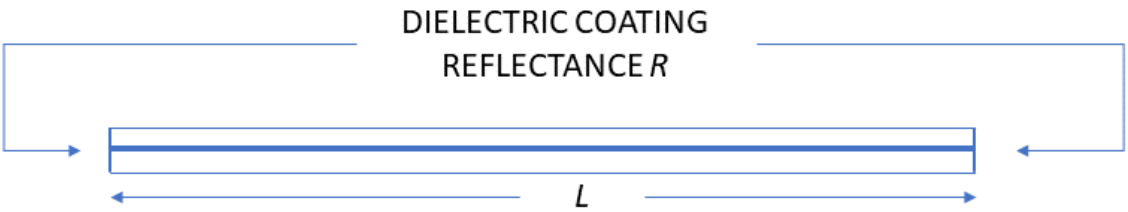

FIGURE 2.1: Scheme of a FP cavity adapted from [27].

The authors explored the sensitivity to temperature of the Fibre Fabry Perot Interferometer (FFPI) for the case where the jacket was not removed of the SMF and the case where it was. They found that the phase sensitivity differed for the two cases. On one

hand, the sensitivity was estimated to be $S_{jacket}\left(phase\right) = 2.2 \cdot 10^{-5}$ rad/°C. On the other hand, they reported that the sensitivity for the case where the nylon jacket was removed of the SMF was $S_{unjacket}\left(phase\right) = 7.9 \cdot 10^{-6}$ rad/°C. Yoshino *et al.* [27] thus concluded that the sensitivity was 2.8 times greater for the first configuration. In the last part of the study the authors utilized the FFPI as a sensor to several physical parameters, including but not limited to magnetic field, acoustic wave and voltage. The deployment of this interferometric configuration introduced to the world the possibility of creating in-fibre FP sensors and also launched the investigation of this type of sensors. Since 1982 much has been done in the field of optical sensing, namely with FP sensors.

In the following year, 1983, Kersey *et al.* further investigated the uses of the FFPI as a sensor and employed a FP cavity whose main objective was to sense acceleration [28]. This FP cavity was composed of an air gap enclosed between two uncoated cleaved end faces of a SMF. As such the monitored interference signal arose from the two back reflections at each interface.

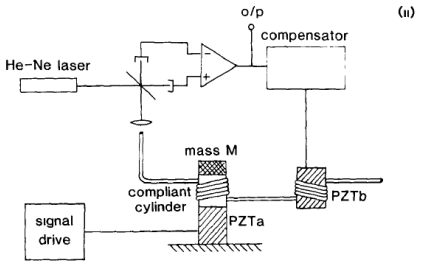

FIGURE 2.2: Accelerometer configuration of a FP sensor adapted from [28].

By 1993, several extrinsic FFPI had been produced. The method of fabrication was simple and cost effective. It consisted of inserting two cleaved optical fibres into a small-diameter tube. Afterwards the cleaved fibres were fusion welded to the tube and fixed in place. The fibres were placed apart from one another to allow the existence of an air gap. Nevertheless, due to the geometric discontinuities between the fibre and the tube the sensor was subjected to strain and therefore was more fragile [29]. To overcome this limitation Kersey *et.al* proposed, in the same year, a novel method of fabricating extrinsic FP cavities [29]. Initially, the authors altered the geometric properties of a silica tubing in order to create a Hollow Core Fibre (HCF) whose outer diameter coincided with that of the SMF and whose inner diameter was estimated to be 70 μm.

Subsequently, one cleaved end face of the custom HCF was fusion spliced to a cleaved end face of a commercial SMF. Before finishing the sensor and splicing the other end face

of the HCF to a second cleaved end face of a SMF, the length of the section of HCF was properly measured with the help of a microscope and the HCF itself was cleaved to the desired sensor length. Finally, as one can see in figure 2.3, a FP sensor with an estimated length of 137 μm had been fabricated.

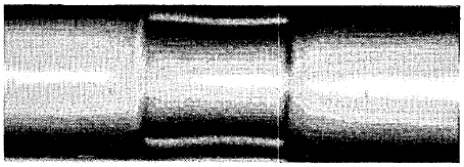

FIGURE 2.3: Photograph of the FP sensor adapted from [29].

In 2004, a intrinsic FP sensor was developed with the goal of strain sensing. First, two SMF were fusion spliced. One SMF had a flat endface and the other had a concave cavity endface. Afterwards by using a small electric furnace the already produced sensor was heated to 850ºC. In that way its length was fine-tuned to the ideal value required to operate in the quadrature point [30].

Further advances in fibre optic sensing were reported in early 2013 when a new sensor was suggested [31]. Although based on the two-wave model like most of the previous developed sensors enumerated here, this sensor stood out due to the fact that prior to forming the sensor one cleaved end face of a SMF was coated with a 50 μm thin film of gold (Au), as seen in figure 2.4. Thereafter, the coated fibre was fusion spliced to an uncoated SMF by means of a commercial fusion splicer. The splice parameters such as arc current and duration were modified to ensure that the Au coating did not evaporate. Nevertheless, after the splicing of the two SMF mentioned above only a 5 nm coating of Au was present. Finally, the uncoated SMF was cleaved a second time thus forming a FP cavity with the desired gauge length. The fields required to form the interference pattern of this FPI emerged from the two reflective surfaces. The first reflection was due to the Au thin film and the second due to the Fresnel reflection arising from the discontinuity of the refractive index.

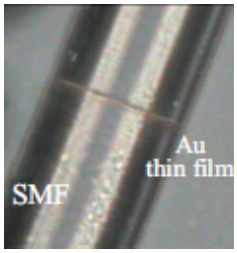

FIGURE 2.4: Figure of the coated SMF adapted from [31].

After production, the interferometer was used as a refractometer. A linear response of the peak power with the external refractive index was verified and a sensitivity of -19.8 dB/Refractive Index Unit (RIU) was reported. In the same way, the sensor was subjected to a shift in temperature in the range $[25, 800]$ºC. Three different cicles of heating and cooling were applied. The sensor demonstrated good repeatibility throughout the 3 cicles. Furthermore, a linear shift of wavelenght with temperature was verified. The estimated sensitivity was 13 pm/ºC. A final stability study was done in which the sensor was put in a thermal bath of 800ºC for 5 hours and the interference dips for a specified wavelength of 1554.2 nm were registered every half hour. The thermal response was constant, *i.e.*, at constant temperature no drift in the interference dip was encountered proving that the sensor had good stability.

In recent years optical sensors were pushed forward. In 2020 a dual-cavity FP interferometric sensor was proposed. Its purpose was to measure simultaneously temperature and high-gas-pressure [32]. One of the cavities was extrinsic and was composed of a small piece of HCF while the other was more complex and made from Photonic Cristal Fibre (PCF). The former was used to sense gas pressure and the latter temperature. The system presented a linear response to the temperature shift in a range of $[40, 1000]$ºC and a sensitivity of 25.3 nm/ºC was reported. The response to pressure also exhibited a linear behaviour in the range of $[0, 10]$ MPa. For the fixed temperature of 40ºC the sensitivity was estimated to be 1460 nm/MPa.

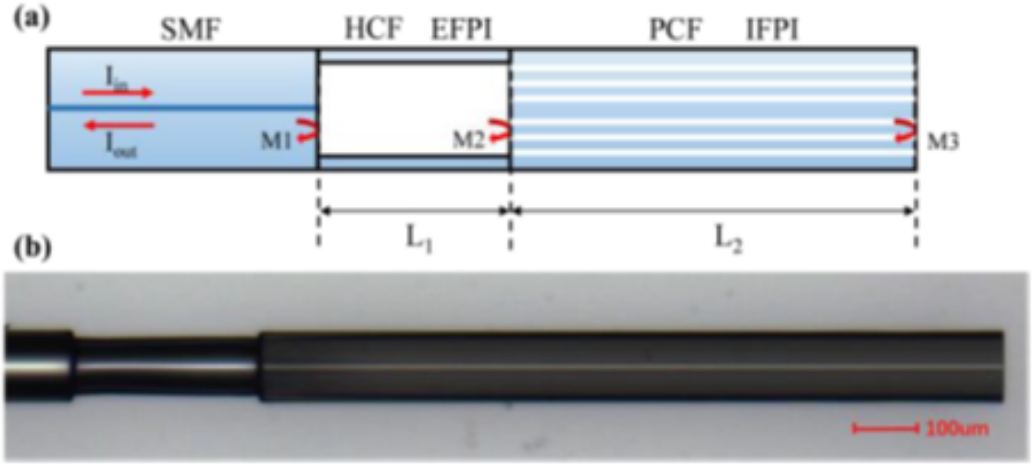

FIGURE 2.5: Image of FP sensor adapted from [32]. In a) it is seen a scheme of the proposed sensor. In b) a microscope image of the sensor is presented.

As seen, optical fibre sensors are used in the most varied applications which are summarised in table 2.1

TABLE 2.1: A summary of several applications of FP sensors and the respective sensitivities to the physical parameters.

Application	Sensitivity
Temperature	$S_{jacket} = 2.2 \cdot 10^{-5}$ rad/°C [27]
Temperature	$S_{unjacket} = 7.9 \cdot 10^{-6}$ rad/°C [27]
Refractive Index	-19.8 dB/RIU [31]
Temperature	13 pm/°C [31]
Temperature	25.3 nm/°C [32]
Gas Pressure	1460 nm/MPa[1] [32]

2.2 Optical Interrogation Systems

2.2.1 Introduction

In the prior section, optical sensors and more specifically FP sensors both in intrinsic and extrinsic form were debated and a few of the many possible uses of this interferometer were listed. Furthermore, in an academic environment, the change of the optical response of these sensors, which is induced by the change of external parameters, is usually monitored via an Optical Spectrum Analyser (OSA). By doing so, the cavity length can also be demodulated. Over the years, novel demodulation methods such as the Fourier transform method [33] and the dual-wavelength method [34] that are able to interrogate an optical sensor and present an alternative to a tradicional OSA were explored and developed.

2.2.2 Brief Review of Interrogation Techniques

Given the importance of the OSA as an established measuring instrument the need to overcome a few of its limitations while making use of the same technology was pressing. Hence, Takanori *et al.* [35], in their work, sucessfully fabricated an OSA which was based on microeletromechanical systems technology and surpassed a traditional OSA due to its 1.7 ms scan speed in the C-band range. Furthermore, the prototype developed OSA had a wavelength resolution of 10 pm.

[1] For a fixed temperature of 40 °C

However, an OSA has its drawbacks such as high cost, high complexity, low speed and inability to be operated *in situ* [36]. Hence, for high frequency signals and for commercial applications this method is not ideal and other viable options are needed.

Therefore, there was a need for low-cost and high speed custom optical interrogators that could be used in commercial applications [17]. Therefore, in late 2017, C.A.R. Díaz *et al.* developed a novel interrogation system which consisted of an in-line FPI. The system was used to interrogate a Fibre Bragg Grating (FBG) sensor [17].

More recently, Jiajian Zheng *et al.* presented their innovative work to the scientific community and reported a novel method to demodulate the length of a FP cavity [18]. The basis for this ingenious method is to monitor the reflected intensities of a two-beam interferometer, I_1 and I_2, for two different wavelengths inputted to the optical Extrinsic Fabry Perot Interferometer (EFPI), *i.e.* λ_1 and λ_2. The reflected intensities are given by the expressions [18]:

$$I_1 = A_0 + B_0 \, cos\left(\frac{4\pi d_0}{\lambda_1}\right) \tag{2.1}$$

$$I_2 = A_0 + B_0 \, cos\left(\frac{4\pi d_0}{\lambda_2}\right) \tag{2.2}$$

where d_0 is the initial length of the FP cavity.

To monitor the variation of the length of the FPI in a fast, cost-effective and straightforward way a differential intensity ratio κ can be defined as[18]:

$$\kappa = \frac{I_{22} - I_{11}}{I_2 - I_1} \tag{2.3}$$

where I_{11} and I_{22} are the reflected intensities for λ_1 and λ_2, respectively, after the variation of the length of the sensor by δd.

For small cavity length variations this intensity ratio has a linear dependence with δd, as seen in equation 2.4 [18].

$$\kappa = \alpha \cdot \delta d + \beta \tag{2.4}$$

where α and β are considered as constants.

Hence, the variation of the FP cavity lenght can be swiftly determined by estimating the value of the parameter κ with the setup from figure 2.6.

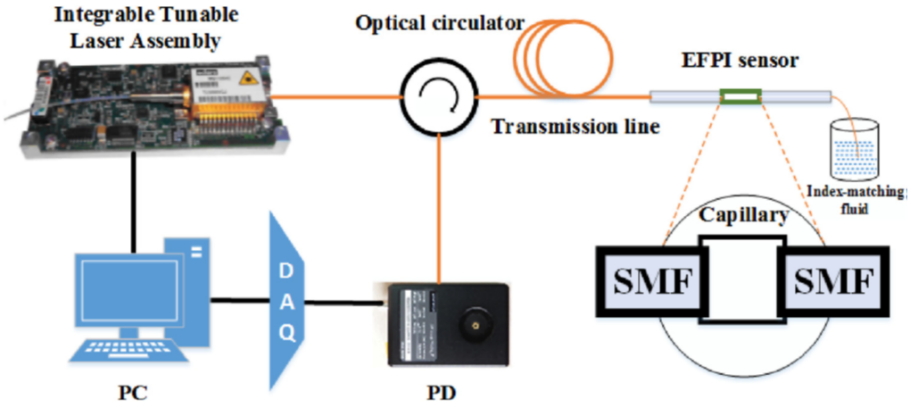

FIGURE 2.6: Scheme of the demodulation setup adapted from [18].

Just last year, further advances in optical interrogation methods were achieved with the works of Quangying Wang *et al.* [16] and Qiang Liu *et al.* [37]. In the first work mentioned above [16] an optical interrogation system based on two cascaded Fibre Sagnac Loops (FSL) was fabricated, as seen in figure 2.7. One of the FSL served as a temperature sensor while the second one was used to interrogate the former. Hence, the Vernier effect, which consists of the interference between two signals from two debalanced interferometers to achieve greater sensitivity to physical parameters was verified.

Subsequently, the signal in the wavelength domain was transposed to the time domain by means of a photodetector and registered in an oscilloscope (OSC in figure 2.7). Aftewards, the signal in the time domain was tracked at the same time that the external environment was altered and the optical length of the first FSL changed. The processing was performed by a Digital Signal Processor. The authors reported that the temperature resolution of the FSL sensor was 1.33×10^{-5} ºC. Furthermore, the whole interrogation system was capable of sensing signals with a frequency as high as 23.5 kHz.

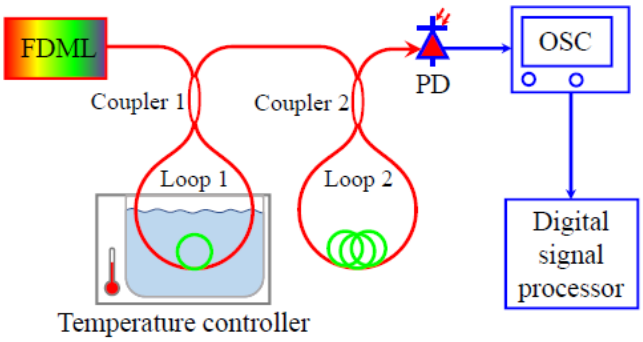

FIGURE 2.7: Schematics of the cascaded Fibre Sagnac Loop setup adapted from [16].

In the following work [37] Qiang Liu *et al.* developed a novel phase shifting white light interferometry method that allowed them to measure, in absolute form, the variation of physical parameters. This complex method begins by registering the reflected intensities of a low-finesse FPI in the frequency domain for two diferent values of the phase (Φ). The reflected intensity and the phase are given by:

$$I(\nu) = A + B\cos(\Phi + \pi) \tag{2.5}$$

$$\Phi = \frac{4n\pi\nu L}{c} \tag{2.6}$$

where c is the speed of light, L is the length of the cavity and ν is the frequency.

The value of Φ is altered by applying a shift in the operating frequency which is made possible by the use of a tunable laser, as shown in equation 2.7.

$$\beta = \frac{4n\pi L}{c}\delta\nu \tag{2.7}$$

where β is a fixed phase bias.

Upon changing the value of Φ throught β the intensity is also changed, as given by equation 2.8. Finally, the well known quadrature phase demodulation algorithm is used to estimate the cavity length.

$$I(\nu) = A + B\cos\left(\frac{4n\pi(\nu+\delta\nu)}{c}L + \pi\right) \tag{2.8}$$

2.3 Concluding Remarks

As reported here much has already been done in the world of optical sensing. Nevertheless, much more can be accomplished and the possibilities in the same are endless.

With each novel work presented to the scientific community more ideas surge and the works complement one another, as it is the case in all of science. On that note, the purpose of this work is to further comprehend the behaviour of optical sensors, namely in-fibre FP sensors, *i.e*, to determine if the length of the FP cavity has any influence on the sensitivity to external parameters. Furthermore, a second part of the present work is the development of an optical interrogation system based on two cascaded FFPI, whose ultimate goal is to measure the variation of physical parameters and more specifically temperature. Hence, one of the cavities serves as a temperature sensor while the second is attached to a Piezoelectric stack (PZT) to form the interrogation system.

Chapter 3

Fundamental Theory

3.1 Introduction

Regarding fibre optical sensors (FOS), there are two main configurations: interferometric sensors and intensity sensors [38]. Interferometric sensors are based, as the name suggests, on light interferometry whilst intensity sensors function by modulating the intensity of light via an external parameter. Light interferometry works by introducing a phase shift between two or more electric fields and then recombining them in order to produce a interference pattern. One can make use of this interference pattern in order to manufacture sensors. If a physical parameter, *i.e.*, the mensurand, induces an additional phase shift there is a change of the optical response of the sensor, *i.e.*, the interference pattern, and by measuring it one can then infer on the physical parameter, after proper calibration.

Despite the fact that intensity based sensors are more simply implemented, can be deployed in a real distributed sensing configuration and are more cost effective than interferometric based sensors [39], interferometric sensors are still more useful than intensity based sensors since the latter present some limitations such as variable losses due to connectors and splices, micro and macro bending loss and mechanical creep. Misalignment of ligth sources and detectors is also a major limitation. Additionally, the interferometric based FOS are more sensitive than intensity-based FOS [40]. Furthermore, intensity based sensors are susceptible to variations of the light source power [39].

Additionally, interferometric sensors themselves can still be subdivided in [41]:

- Two-wave Interferometric Sensors;

- Multi-wave Interferometric Sensors.

Most fall in the first subcategory such as Mach Zender, Michelson, Sagnac [42]. Notwithstanding, there are a few interferometers that by nature have a multi-wave interferometry behaviour. One of the most well known interferometers of the second configuration is the Fabry Perot interferometer (FPI) [7].

3.2 Fresnel Coefficients

When a light beam is incident on a surface, there are two processes that can happen, as shown in figure 3.1. The electric field associated to the light beam can be transmitted or reflected. Associated with these phenomena, one can define parameters that describe them. These parameters are denominated as coefficient of reflection (r) and coefficient of transmission (t). Nevertheless, due to the polarization of the light beam care must be taken in defining these coefficients. Thusly, the two following pair of equations explain the reflected and transmitted behaviour of p-polarized waves and s-polarized waves, respectively [43].

$$r_p = \frac{n_2 \cos(\theta_1) - n_1 \cos(\theta_2)}{n_2 \cos(\theta_1) + n_1 \cos(\theta_2)} \tag{3.1}$$

$$t_p = \frac{2\, n_1 \cos(\theta_1)}{n_2 \cos(\theta_1) + n_1 \cos(\theta_2)} \tag{3.2}$$

$$r_s = \frac{n_1 \cos(\theta_1) - n_2 \cos(\theta_2)}{n_1 \cos(\theta_1) + n_2 \cos(\theta_2)} \tag{3.3}$$

$$t_s = \frac{2\, n_1 \cos(\theta_1)}{n_1 \cos(\theta_1) + n_2 \cos(\theta_2)} \tag{3.4}$$

where n_1 and n_2 are the refractive index of the first medium and second medium respectively and θ_1 and θ_2 are the angle of incidence and transmission, respectively, as defined by Snell laws of reflection and depicted in figure 3.1.

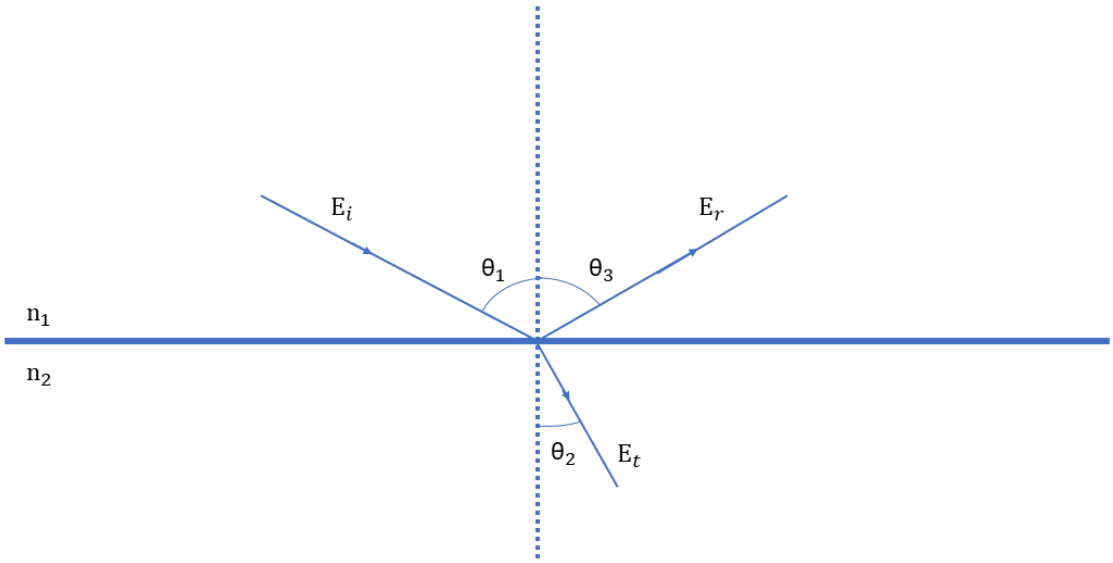

FIGURE 3.1: Electric field behaviour upon incidence in an interface.

For the special case of normal incidence, *i.e.*, $\theta_1 = 0$, the laws of reflection say that $\cos(\theta_1) = \cos(\theta_2) = 1$. Therefore, the above equations $(3.1 - 3.4)$ can be rewritten in a much simpler form, as seen in equations $(3.5 - 3.8)$:

$$r_p = \frac{n_2 - n_1}{n_2 + n_1} \tag{3.5}$$

$$t_p = \frac{2\,n_1}{n_2 + n_1} \tag{3.6}$$

$$r_s = \frac{n_1 - n_2}{n_1 + n_2} \tag{3.7}$$

$$t_s = \frac{2\,n_1}{n_1 + n_2} \tag{3.8}$$

When dealing with unpolarized light waves the coefficients of reflection and transmission for the two polarizations must be used.

3.3 Optical Sensors

3.3.1 Fabry Perot Interferometers

As seen in figure 3.2, a FPI consists of two parallel reflective surfaces which separate two mediums with different refractive indexes. The incident electric field is transmitted and reflected at the first interface. After being transmitted, if the interfaces have a high coefficient of reflection, the electric field present in the medium is constantly reflected and transmitted at the interfaces. Thus the conditions for multi wave interference are met.

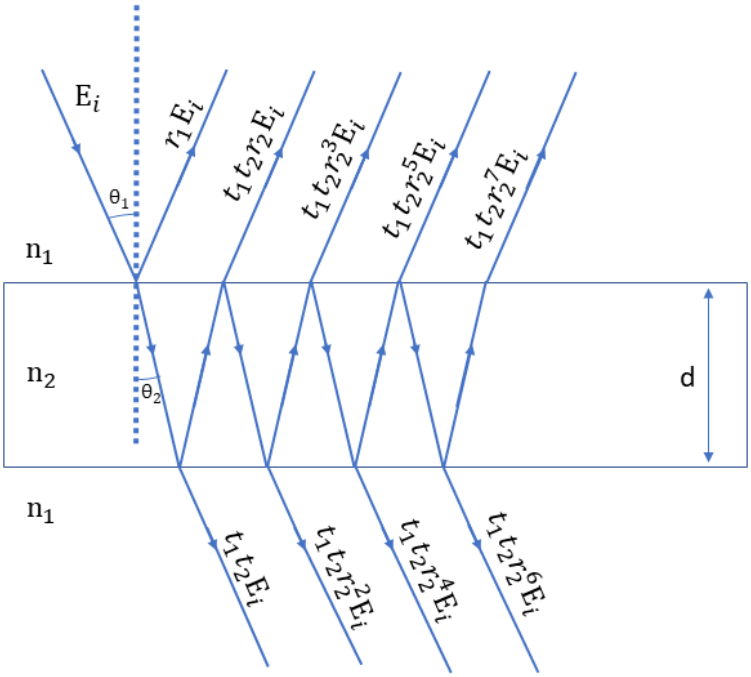

FIGURE 3.2: Scheme of a bulk FP interferometer adapted from [43].

Assuming, for simplicity, that the light is linearly polarized, the subscript in the equations $(3.1 - 3.4)$ can be dropped and the coefficients of reflection and transmission are defined as r and t. Using the scheme of figure 3.2, the nomenclature mentioned above and the principle of superposition, which says that the resultant electric field is the sum of all existent electric fields, it is now possible to calculate the reflected electric field [43], as seen in equation 3.9.

$$\overrightarrow{E_r} = \sum_{N=1}^{\infty} \left(t_1 t_2 r_2^{(2N-3)} \right) \cdot e^{i\left[-(N-1)\delta\right]} \overrightarrow{E_i} \tag{3.9}$$

where t_1 is the coefficient of transmission when the electric field of the beam is transmitted from the medium with refractive index n_1 to the medium with refractive index n_2. Additionally t_2 and r_2 are the coefficients of transmission and reflection when the electric field of the beam is transmitted from the medium with refractive index n_2 to the medium with refractive index n_1. Furthermore, δ is defined as the phase diference between two consecutive beams inside the medium with refractive index n_2 and is given by equation 3.10.

$$\delta = k\Delta \tag{3.10}$$

where k and Δ are, respectively, the wavevector of the electric field and the optical length of the beam. They are defined as:

$$\Delta = 2\, n_2\, d \cos\left(\theta_2\right) \tag{3.11}$$

$$k = \frac{2\pi}{\lambda} \tag{3.12}$$

where d is the lenght of the interferometer, θ_2 is the angle of refraction and λ is the wavelength of the light associated with the electric field.

The sum in equation 3.9 gives the expression for the reflected electric field, which is presented in equation 3.13.

$$\overrightarrow{E_r} = \left[\frac{r_2\left(1 - e^{-i\delta}\right)}{1 - r_2^2\, e^{-i\delta}}\right] \overrightarrow{E_i} \tag{3.13}$$

Nevertheless, since nowadays it is unfeasible to measure electric fields due to their high frequency the measured quantity of interest is the time average of the electric field, *i.e.*, the irradiance, which is defined as [43]:

$$I\left(\overrightarrow{r}, t\right) = \left\langle \overrightarrow{E}\left(\overrightarrow{r}, t\right) \cdot \overrightarrow{E^*}\left(\overrightarrow{r}, t\right) \right\rangle \tag{3.14}$$

Taking into account that in our model both reflective surfaces exhibit the same coefficient of reflection the reflected irradiance spectrum (I_R) has the following form [43]:

$$I_R = \left[\frac{2R\left(1 - \cos\left(\delta\right)\right)}{1 + R^2 - 2R\cos\left(\delta\right)}\right] I_I \tag{3.15}$$

where I_I is the irradiance of the incident electric field and $R = r_2^2$.

Considering that in our model the absorption at the interface between the two different medium and at the medium with refractive index n_2 is null, in addition to the assumptions already made an expression for the transmitted irradiance (I_T) can also be derived at the cost of the reflected irradiance, since for our model:

$$I_R + I_T = I_I \tag{3.16}$$

Thus the transmitted irradiance, which is better known as the Airy Function is given by equation 3.17 [43].

$$I_T = \frac{\left(1 - R\right)^2}{1 + R^2 - 2R\,\cos\left(\delta\right)} I_I \tag{3.17}$$

For simplicity, it is considered that the angle of incidence of the electric field on the interface is 0°. Hence, by the laws of reflection the angle of refraction of the transmitted

electric field (θ_2) is also 0^o and $\cos(\theta_2) = 1$. By substituting equation 3.10 in equations 3.15 and 3.17 and making use of equation 3.11 the following expressions are obtained:

$$\frac{I_R}{I_I} = \left[\frac{2R\left(1-\cos\left(2kn_2d\right)\right)}{1+R^2-2R\cos\left(2kn_2d\right)}\right] \tag{3.18}$$

$$\frac{I_T}{I_I} = \frac{(1-R)^2}{1+R^2-2R\cos\left(2kn_2d\right)} \tag{3.19}$$

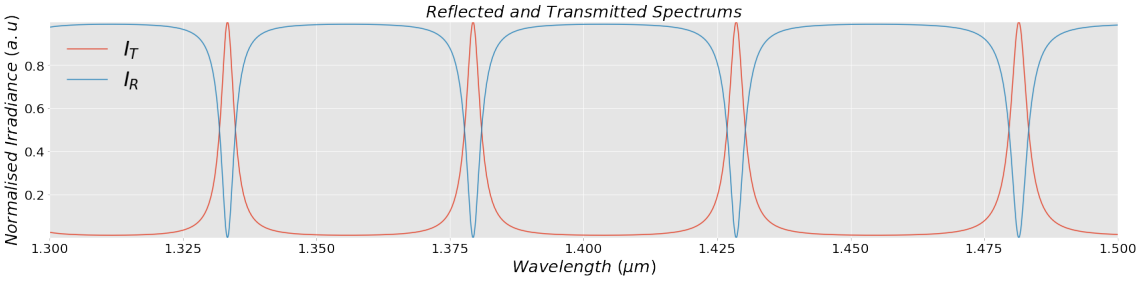

FIGURE 3.3: Transmission and Reflected Spectrum for r = 90%.

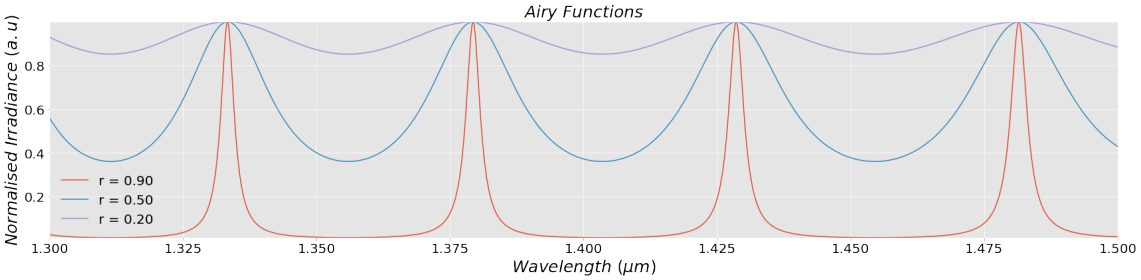

FIGURE 3.4: Transmission spectrum for three different coefficients of reflection, namely r = 90%, 50%, 20%.

In figure 3.3 the transmitted and reflected irradiance spectrums are displayed for the same value of the coefficient of reflection, *i.e.*, $r = 90\%$. It is evident the conservation of energy and the existence of a minimum of the transmitted irradiance spectrum and a maximum of the reflected irradiance spectrum for the same wavelenght and vice-versa.

In figure 3.4 the transmitted irradiance spectrum is visible for three diferent values of the coefficient of reflection, namely $r = 90\%, 50\%$, and 20%. This illustrates the importance of the latter in the transfer function of a Fabry Perot (FP) cavity, *i.e.*, equation 3.19. Given the importance of the coefficient of reflection of the electric field for a FPI a coefficient of Finesse (F), that depends on r and hence on R was defined, as seen in equation 3.20.

$$F = \left[\frac{4R}{(1-R)^2} \right] \tag{3.20}$$

An additional important figure of merit of a FPI is the Free Spectral Range (FSR). The FSR is defined as the separation between neighbouring peaks and is therefore closely related to the resolution of the FPI, *i.e.*, the minimum separation of wavelengths that the FPI can discerne. From equation 3.18 the FSR can be calculated and the resulting expression is given by equation 3.21 [44].

$$FSR = \frac{\lambda_1 \lambda_2}{2\, n_2\, d} \tag{3.21}$$

where λ_1 and λ_2 are the wavelengths of the peaks.

3.3.1.1 In-fibre Fabry Perot Interferometers

Nowadays, however, most FPI are made in-fibre. They can be further separated in extrinsic and intrinsic interferometers. On one hand, extrinsic interferometers are interferometers in which the mensurand acts on an external part of the optical fibre and the latter has the sole purpose of propagating the light to the region of interest, *i.e.*, the sensor. On the other hand, in intrinsic sensors the mensurand acts on the fibre and therefore the fibre itself transforms into the sensor.

In figure 3.5 a scheme of an extrinsic FPI is shown. The FP sensor is composed of a hollow core fibre (HCF) enclosed between two single mode fibres (SMF). The light is propagated by the SMF to the sensing region, *i.e*, the HCF. Any alteration of the optical length of the HCF results in a change of the reflected irradiance.

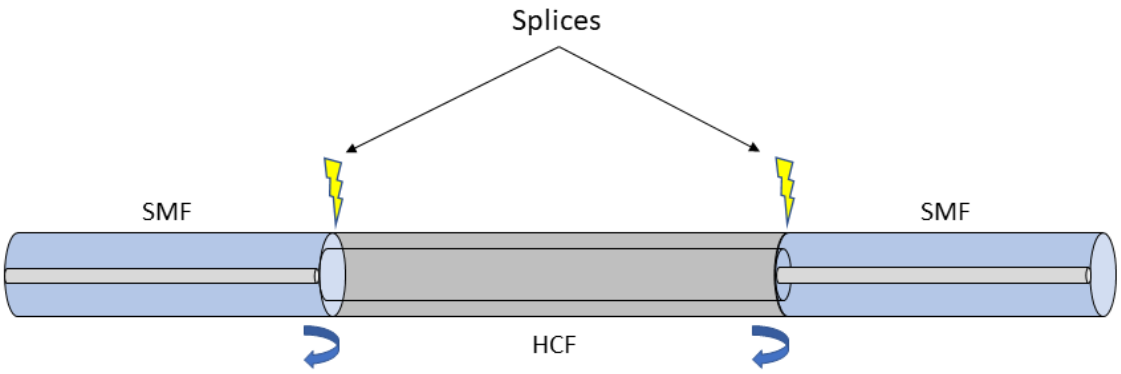

FIGURE 3.5: Scheme of a low finesse Fabry Perot sensor.

In the interfaces SMF-HCF and HCF-SMF depicted in figure 3.5, there is a discontinuity of the refractive index. Because of this discontinuity two reflected beams are created,

one in each interface. The theoretical reflectivity is low, approximately 4%. Hence, the two-wave model is used and the interferometer is said to be of low finesse. The two wave model consists of using only the first reflections of the interfaces SMF-HCF and HCF-SMF, since the power contained in further reflected beams is negligible. Thus, those beams do not have any substantial contribution to the interference pattern.

Since in optical fibres the angle of incidence is normal to the interface that separates the two mediums, one can use the equations $(3.5 - 3.8)$ to calculate the electric field of interest, assuming that absorption losses are not present in our model. Additionally, the light that propagates in the optical fibre is usually unpolarized due to the properties of the light source in use. Therefore, both polarizations must be taken into account and the resultant electric field is given by equation 3.22.

$$\overrightarrow{E_{out}} = \overrightarrow{E_{out_p}} + \overrightarrow{E_{out_s}} \tag{3.22}$$

where $\overrightarrow{E_{out_p}}$ is given by

$$\overrightarrow{E_{out_p}} = \left[r_p + t_p^2 \cdot r_p \cdot \exp\left[i \cdot (\phi + \pi) \right] \right] \overrightarrow{E_{in_p}} \tag{3.23}$$

and $\overrightarrow{E_{out_s}}$ is given by:

$$\overrightarrow{E_{out_s}} = \left[r_s + t_s^2 \cdot r_s \cdot \exp\left[i \cdot (\phi + \pi) \right] \right] \overrightarrow{E_{in_s}} \tag{3.24}$$

where ϕ is the phase shift between the two electric fields given by equation 3.25.

$$\phi = 2\beta L \tag{3.25}$$

The electric field is incident on the interface HCF-SMF from a medium with lower refractive index on a medium with a higher refractive index. Hence the coefficient of reflection is negative and a additional phase of π is present. Since $e^{i\pi}$ = -1, equations 3.23 and 3.24 can be written as:

$$\overrightarrow{E_{out_p}} = \left[r_p - t_p^2 \cdot r_p \cdot \exp\left(i \cdot \phi \right) \right] \overrightarrow{E_{in_p}} \tag{3.26}$$

$$\overrightarrow{E_{out_s}} = \left[r_s - t_s^2 \cdot r_s \cdot \exp\left(i \cdot \phi \right) \right] \overrightarrow{E_{in_s}} \tag{3.27}$$

Since for normal incidence $r_p = -r_s$ and $t_p = t_s$ the resultant electric field can be rewritten in a simpler form:

$$\overrightarrow{E_{out}} = r_p \left(\overrightarrow{E_{in_p}} - \overrightarrow{E_{in_s}} \right) - r_p \cdot t_p^2 \cdot \exp\left(i \cdot \phi \right) \left(\overrightarrow{E_{in_p}} - \overrightarrow{E_{in_s}} \right) \tag{3.28}$$

For simplicity r_p and t_p^2 can be defined, respectively, as A and B. Then, the reflected electric field is expressed as:

$$\overrightarrow{E_{out}} = A\left(\overrightarrow{E_{in_p}} - \overrightarrow{E_{in_s}}\right) - B \cdot \exp\left(i \cdot \phi\right)\left(\overrightarrow{E_{in_p}} - \overrightarrow{E_{in_s}}\right) \tag{3.29}$$

Using equation 3.14 the measured signal can be calculated (see Appendix A) and the resulting equation is:

$$I_R = \left[A^2 + B^2 - 2\,A\,B\,\cos\left(\phi\right)\right] I_I \tag{3.30}$$

Substituing equation 3.25 in equation 3.30, one finally obtains:

$$I_R = \left[A^2 + B^2 - 2\,A\,B\,\cos\left(2\beta L\right)\right] I_I \tag{3.31}$$

Hence, as seen in equation 3.31 the reflection spectrum is altered to a sinusoidal signal.

By noting that β is the effective wavevector and therefore is related to the effective refractive index of the sensor by $\beta = n\,k = \frac{2n\pi}{\lambda}$, the above equation (3.31) is rearranged in the following form:

$$I_R = \left[A^2 + B^2 - 2\,A\,B\,\cos\left(\frac{4n\pi L}{\lambda}\right)\right] I_I \tag{3.32}$$

where L is the length of the interferometer, n is the refractive index and λ is the wavelength in air. This signal is represented in figure 3.6.

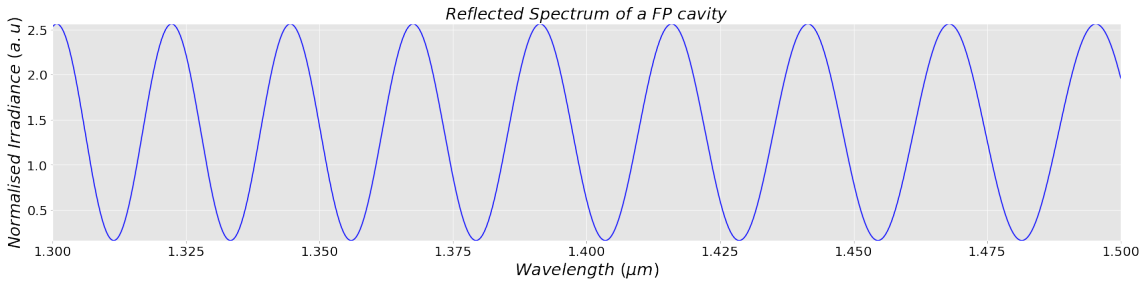

FIGURE 3.6: Reflected Irradiance of a in-fibre FP cavity.

Equation 3.32 can be rewritten in the more familiar form as:

$$I_R = \left[I_1 + I_2 - 2\sqrt[2]{I_1 I_2}\cos\left(\frac{4n\pi L}{\lambda}\right)\right] \tag{3.33}$$

where I_1 and I_2 are the reflected irradiance of the first and second beams, respectively. Furthermore, since the visibility can be defined as [45]:

$$V = \frac{2\sqrt[2]{I_1 I_2}}{I_1 + I_2} \tag{3.34}$$

equation 3.35 can be rearranged as:

$$\frac{I_R}{I_1 + I_2} = \left[1 - V\cos\left(\frac{4n\pi L}{\lambda}\right)\right]. \tag{3.35}$$

3.4 Optical Interrogation Model

Our proposed interrogation system consists of a FP cavity with a dinamically varying optical length as the physical length of the cavity is mechanically varied by the aid of a Piezoelectric stack (PZT). This FP cavity is in tandem with another FP cavity, as can be seen in figure 3.7.

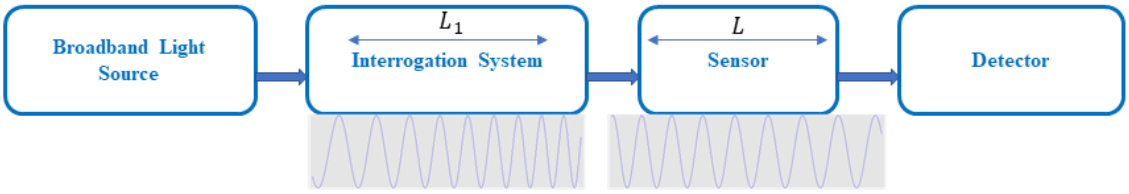

FIGURE 3.7: Scheme of the setup consisting of the optical interrogation system and the FP sensor.

For simplicity in the calculations, an arbitrary incident electric field $\overrightarrow{E_0}$ will be considered and polarization effects will not be taken into account. Furthermore, arbitrary coefficients to describe the phenomenona of reflection, *i.e.*, the coefficients of reflection, will be used, namely A, B, A_1 and B_1.

The first FP cavity modulates the incident electric field. Therefore, the output signal of the first cavity is:

$$\overrightarrow{E} = \left[A + B\,e^{i(\phi+\pi)}\right]\overrightarrow{E_0} \tag{3.36}$$

The modulated field will be further modulated by the second cavity. The final reflected field is thus given by:

$$\overrightarrow{E_R} = \left[A_1 + B_1\,e^{i(\phi_1+\pi)}\right]\overrightarrow{E} \tag{3.37}$$

where

$$\phi = 2\beta L \tag{3.38}$$

and

$$\phi_1 = 2\beta L_1 \tag{3.39}$$

Substituting equation 3.36 in equation 3.37, the expression for the final reflected electric field is:

$$\overrightarrow{E_R} = \left[A_1 + B_1\, e^{i(\phi_1+\pi)}\right]\left[A + B\, e^{i(\phi+\pi)}\right]\overrightarrow{E_0} \tag{3.40}$$

Equation 3.40 can be simplified to give:

$$\overrightarrow{E_R} = \left(AA_1 - AB_1\, e^{i\phi_1} - A_1B\, e^{i\phi} + BB_1\, e^{i(\phi_1+\phi)}\right)\overrightarrow{E_0} \tag{3.41}$$

The reflected irradiance which was derived in Appendix B is given by:

$$\begin{aligned}\frac{I_{out}}{I_{in}} &= C \\ &- C_1 \cdot \cos(\phi) \\ &- C_2 \cdot \cos(\phi_1) \\ &+ C_3\left[\cos(\phi_1 + \phi) + \cos(\phi_1 - \phi)\right]\end{aligned} \tag{3.42}$$

where

$$\begin{aligned}C &= A^2 \cdot A_1^2 + A^2 \cdot B_1^2 + A_1^2 \cdot B^2 + B^2 \cdot B_1^2, \\ C_1 &= 2\left(AA_1^2B + ABB_1^2\right), \\ C_2 &= 2\left(A^2A_1B_1 + A_1B^2B_1\right), \\ C_3 &= 2AA_1BB_1\end{aligned}$$

In equation 3.42 cosine terms with the frequencies $\phi_1 + \phi$ and $\phi_1 - \phi$ appear. Therefore, the interrogation system is heterodine. When the cavities have different optical lengths they are not in phase. Since they are not in phase but have similar frequencies an optical beat is expected. The optical beat phenomenon is illustrated in figure 3.8.

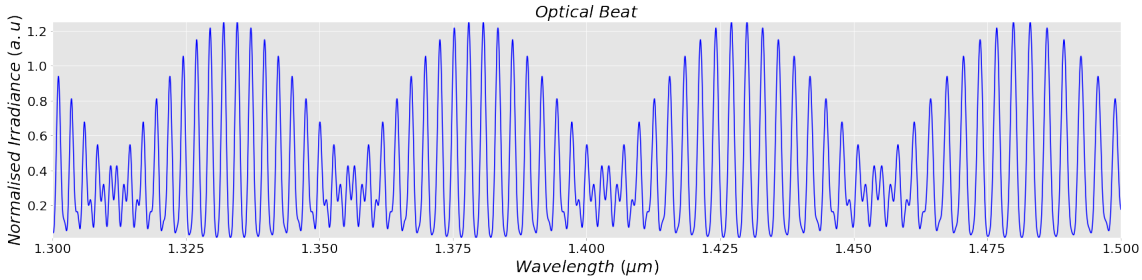

FIGURE 3.8: Optical spectrum from two unbalanced FP cavities. A optical beat phenomenon between two FPI is observed.

When the cavities are balanced, *i.e.*, have the same optical length the frequencies are identical. Therefore $\phi_1 = \phi$ and the irradiance signal from equation 3.42 is reduced to:

$$\frac{I_{out}}{I_{in}} = \left[C - 2\cdot(C_1 + C_2)\cos(\phi) + C_3\cos(2\cdot\phi) + C_3\right] \tag{3.43}$$

Noting that $\cos(2 \cdot \phi) = 2\cos^2(\phi) - 1$, equation 3.43 can be rewritten in the following form:

$$\frac{I_{out}}{I_{in}} = \left[C - 2 \cdot (C_1 + C_2)\cos(\phi) + 2C_3\cos^2(\phi)\right] \tag{3.44}$$

Hence, two frequencies are present in the signal displayed in figure 3.9 and the second frequency is the double of the first. Hence, an interference between the two signals is still present. However, the beat phenomenon is absent as the beat frequency, *i.e.*, $\phi_1 - \phi$ is zero.

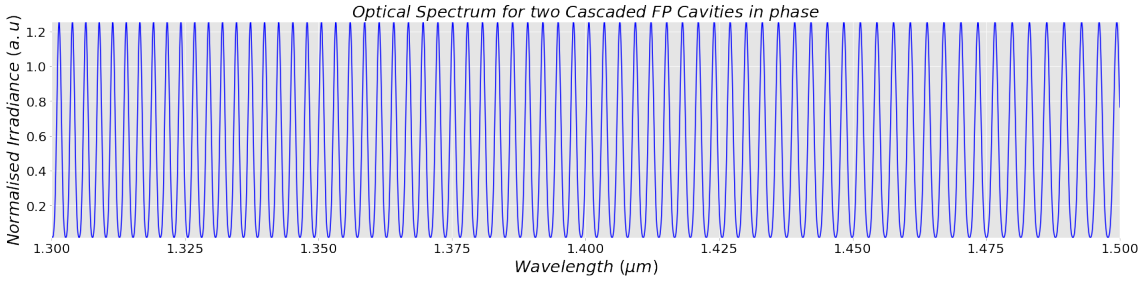

FIGURE 3.9: Spectrum of two balanced FP cavities. The two FP have the same length. Therefore the optical beat phenomenon is no longer present.

3.4.1 Behaviour in the time domain

The cross correlation of the response of the two FP cavities, *i.e.*, the integral of the optical beat, which was derived in Appendix C, is given by equation 3.45.

$$I_{out}(t) = \int_{\beta_1}^{\beta_2} I_{out}(\beta)\, d\beta \tag{3.45}$$

The resultant expression for the case where the source has a flat spectrum is presented in figure 3.12 and is given by:

$$\begin{aligned} I_{out}(t) &= I_{in}(\beta) \cdot [C \cdot [\beta_2 - \beta_1] \\ &- C_1 \cdot \left[\beta_2 \cdot sinc(2\beta_2 L) - \beta_1 \cdot sinc(2\beta_1 L)\right] \\ &- C_2 \cdot \left[\beta_2 \cdot sinc(2\beta_2 L_1(t)) - \beta_1 \cdot sinc(2\beta_1 L_1(t))\right] \\ &+ C_3 \cdot \beta_2 \cdot \left[sinc\left[2\beta_2 (L_1(t) + L)\right] + sinc\left[2\beta_2 (L_1(t) - L)\right]\right] \\ &+ C_3 \cdot \beta_1 \cdot \left[sinc\left[2\beta_1 (L_1(t) + L)\right] + sinc\left[2\beta_1 (L_1(t) - L)\right]\right]] \end{aligned} \tag{3.46}$$

Two sources with a different spectrum were considered in the model and their influence on the cross correlation signal was verified. The sources considered had a flat and gaussian spectrum which are displayed in figures 3.10 and 3.11.

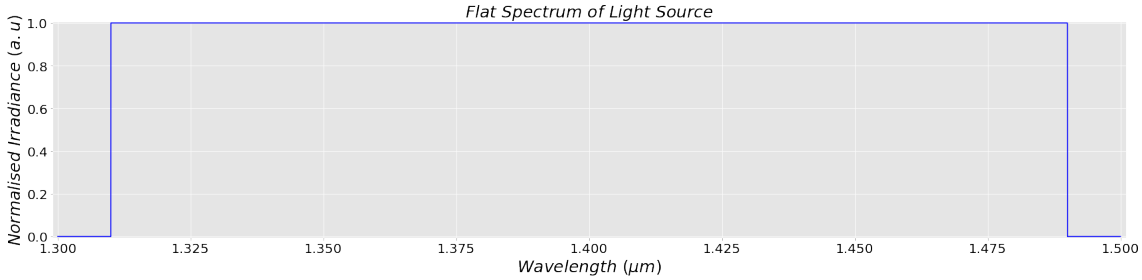

FIGURE 3.10: Spectrum of a flat source

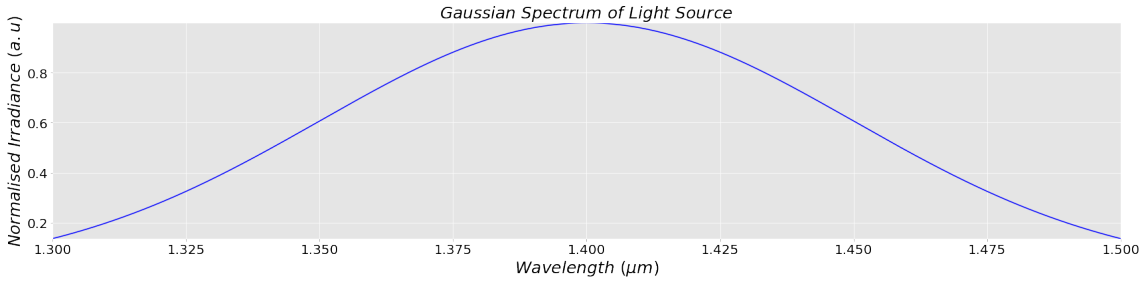

FIGURE 3.11: Spectrum of a gaussian source. The parameters of the gaussian considered were a = 1.0, b = 1.4, c = 0.05. a, b, c are the amplitude, the center of the gaussian and the standard deviation, respectively.

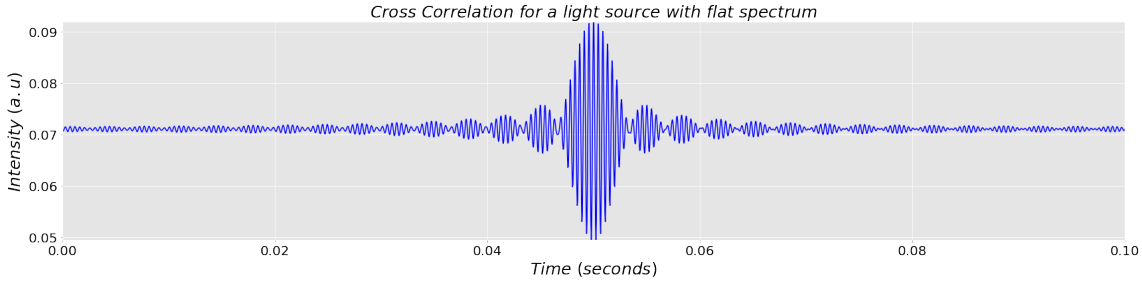

FIGURE 3.12: Cross Correlation signal for a source with flat spectrum. A central sinc with side lobes is observed.

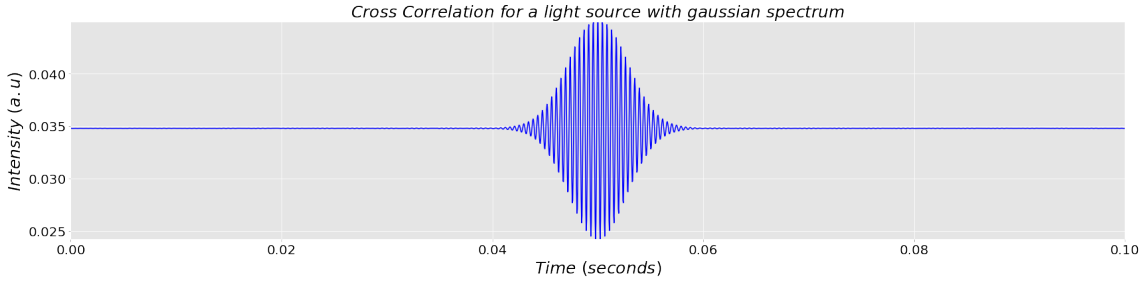

FIGURE 3.13: Cross Correlation signal for a source with gaussian spectrum. When using a source with gaussian spectrum, the side lobes disappear.

In figures 3.12 and 3.13 the numeric simulation of the cross correlation signal considering a source with a square power spectrum and a source with a gaussian power spectrum

are presented. It is advantageous to use the source with a gaussian spectrum since the side lobes are no longer present and is therefore easier to monitor the shift of the signal.

3.5 Concluding Remarks

In this chapter, the necessary theory to understand FP cavities was described. The two wave model was presented and low finesse in-fibre FPI were discussed and explained. Furthermore, the main equations that govern the behaviour of the aforementioned sensors were derived. Afterwards, we make use of the derived equations to predict the optical spectrum of an interrogation system that is based on two cascaded FP cavities. The behaviour of the spectrum was analysed for two cases. In the first case the cavities were unbalanced and an optical beat was observed. In the second case the cavities were in phase. Therefore, the optical beat is no longer present and the resultant signal includes a signal with two frequencies where the second frequency is an harmonic of the first. Finally, the optical response is integrated in wavelength. Since the length of one of the cavities is a function of time the spectrum of the two cascaded cavities is transposed to the time domain. The influence of the spectrum of the light source on the cross correlation of the two cavities is investigated and discussed.

Chapter 4

Fabrication and Characterization of Fabry-Perot Sensors

4.1 Introduction

In this chapter the first work carried out within the scope of this thesis is presented. Initially, a detailed description of the Fabry Perot (FP) cavity manufacturing process is discussed. Afterwards, the already fabricated sensors were characterized in strain and temperature as an Optical Spectrum Analyser (OSA) was used to monitor the optical response of the FP sensor to external parameters. Finally, a study of the dependence of the sensitivity to external parameters with the length of the sensor is carried out.

4.2 Fabrication of FP Sensors

In this work the fabrication process of FP cavities consisted of enclosing a hollow core fibre (HCF) that has a unitary refractive index, a external diameter of 125 micrometers and an internal diameter of 75 micrometers between two single mode fibres (SMF) which have a cladding of 125 micrometers, a core of 8 micrometers and an effective refractive index of 1.44. This process is depicted in figure 4.1. Initially both the SMF and the HCF were cleaved with a Fitel S323 optical fibre cleaver. Hence the ends were properly cut in a transversal direction to the optical fibre axis and ready to be spliced, as seen in figure 4.1 a). Afterwards, using a Sumitomo Electric Type 72-C fusion splicer an electric arc was applied between the SMF and the HCF through the use of two electrodes, as seen in figure 4.1 b). The electric arc should be applied at the interface between the SMF and HCF.

However it was realized near the interface but on top of the SMF to prevent the collapse of the HCF. This allowed for a more controlled splice where the interface between the mediums with different refractive indexes remained perpendicular to the optical fibre axis. In order to create the splice between those different tipes of fibres the manual mode of the fusion splicer was used with an arc time of 1.00 seconds and a arc power of Standard -75. The induced electric arc caused a temperature increase on the splice region. Due to this increase the SMF and HCF were melted together and consequently became spliced.

In order to control with greater precision the length of the FP sensor in the manufacturing process the fibre cleaver was positioned on a manual translation stage while simultaneously placing the fibre in fibre clamps. The whole process was monitored by a digital camera in conjunction with a magnifying glass. The digital camera was used to properly place the endface of the HCF at the desired position where the second cleaving was executed, as can be seen in figure 4.1 c).

Afterwards, the final splice needed to fabricate the sensor was carried out as one can see in figure 4.1 d). This splice was identical to the first, *i.e.*, the manual mode was again used with the same parameters as before. Thus, in the end, a structure with the desired gauge length was fabricated, as seen in figure 4.1 e).

The process described above was vital in the production of all FP sensors used during this work. The sensors shared the same characteristics apart from length since the range of lengths for the aforementioned sensors goes from 30 to 1200 μm.

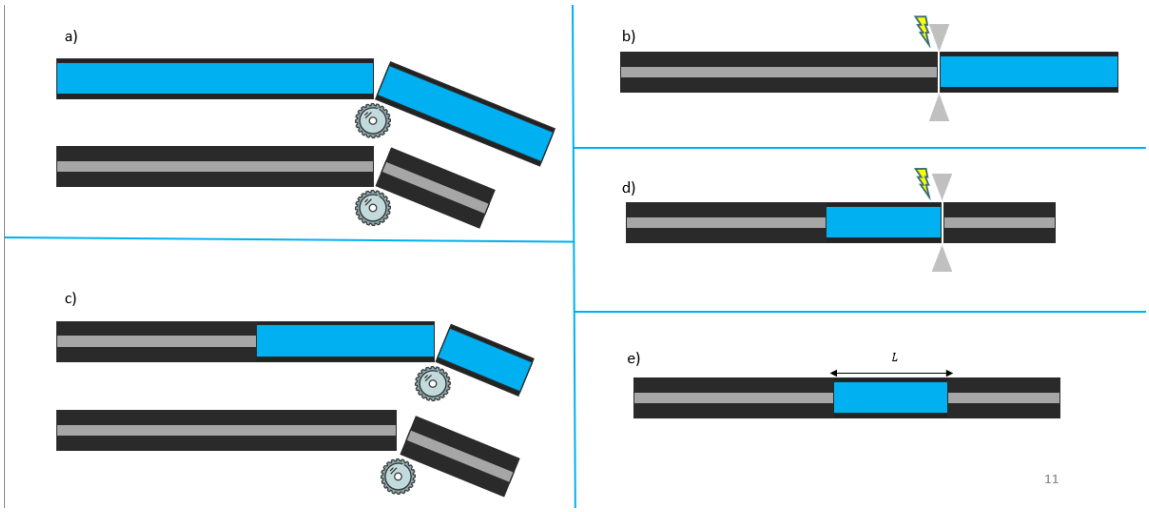

FIGURE 4.1: Method of fabrication of FP cavities.

Afterwards, all the FP sensors were taken to a Leica DM500 Microscope Camera with magnifying powers of 4x, 20x and 50x such that the length of the sensor could be verified.

This assured that all fabricated FP sensors had different lengths, as can be seen in figure 4.2, where two FP sensors with respective lengths of L = 238.25 μm and L = 41.72 μm are shown.

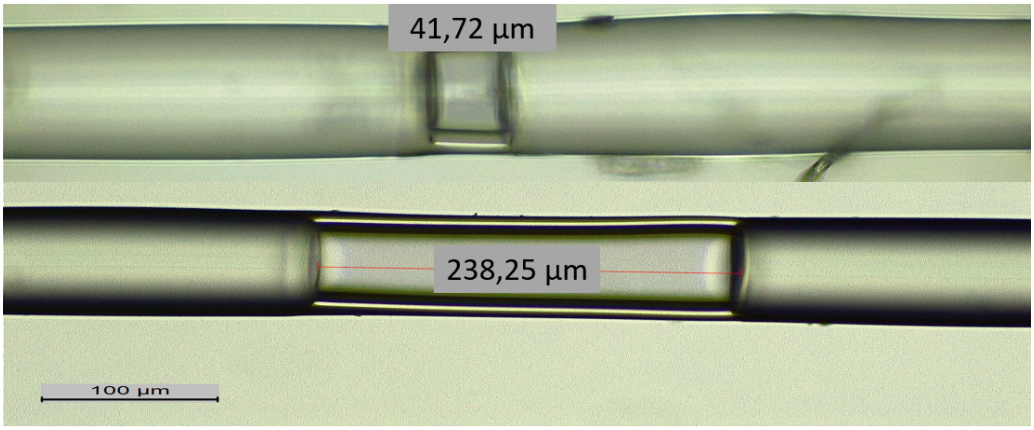

FIGURE 4.2: Two FP cavities with different lengths. One has a length of 41.72 μm and the another has the length of 238.25 μm.

4.3 Characterization of FP sensors with different length

Whilst the FP cavities were produced the spectral response of each sensor was acquired via an OSA and the Free Spectral Range (FSR) registered. Hence, resorting to equation 3.21, the already determined length could be confirmed with greater accuracy.

To register the spectrum of the FP cavity a broadband source, a three-port circulator and an OSA were used. Connected to port 1, 2 and 3 of the circulator were the broadband light source, the FP cavity and the OSA, respectively. The broadband light source, which was centered around 1570 nm and had a bandwidth of 70 nm was used to inject light in the optical fibre. The light was propagated from port 1 of the circulator to port 2. After encountering the FP sensor the light was reflected back to port 2 and propagated to port 3 where it was finally detected by the OSA. The spectrum of the reflected light was sinusoidal as predicted by the transfer equation of the system, *i.e.*, equation 3.32.

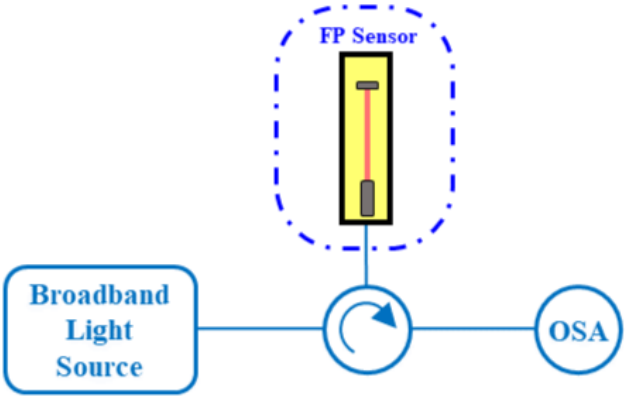

FIGURE 4.3: Scheme of the setup of the acquisition of the optical spectrum.

4.3.1 Strain Characterization

The setup from figure 4.3 was used together with the setup from 4.4 to monitor and record the reflected spectrum of the FP cavity as strain was induced in the sensor.

As can be seen in the scheme of figure 4.4, one portion of cladded optical fibre was fixed with an acrylic adhesive to a platform. Additionally another portion of the fibre was fixed with the same adhesive to a micro-translation stage. During this process, one had to make sure that the optical fibre was tensed and that the sensing region of the optical fibre was located between the two points of contact. After this process the distance between the two points of contact, namely L_0, was measured with a ruler and recorded. The distance between the points of contact was always the same for every FP cavity to assure uniformity of the study, *i.e.*, $L_0 = (400.0 \pm 0.5)$ mm.

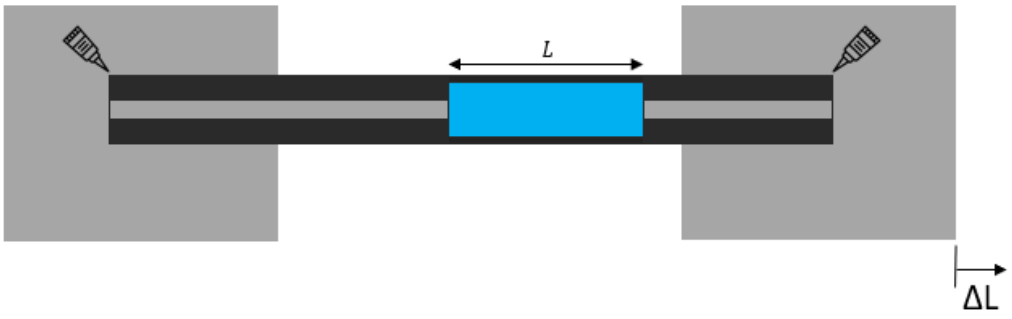

FIGURE 4.4: Setup used to characterize FP cavities.

The micro-translation stage was moved from its initial position to a maximum of 550 μm with a 50 μm step. Under the conditions of ambient temperature, the whole fibre was

stretched and the additional displacement, *i.e.*, ΔL, recorded. Since the fibre was previously tensed before the stretching it is assumed that the additional displacement of the sensing region is identical to the displacement of the micro-translation stage. Therefore the sensing region is displaced by ΔL and thus strain is induced on the sensor which can be calculated by the formula [46]:

$$\epsilon = \frac{\Delta L}{L_0} \tag{4.1}$$

According to equation 3.32 the reflected spectrum is subject to a phase shift and the wavelengths for which there is resonance, *i.e.*, peaks of reflection are going to differ. As can be seen in figure 4.5, more than one reflection peak exists. Therefore, a zoom was made on the graphic from figure 4.5 in the range of wavelengths $[1555, 1570]$ nm. Hence, the redshift of the spectrum for a FP cavity with a length of 41.72 μm can be better seen in the figure 4.6.

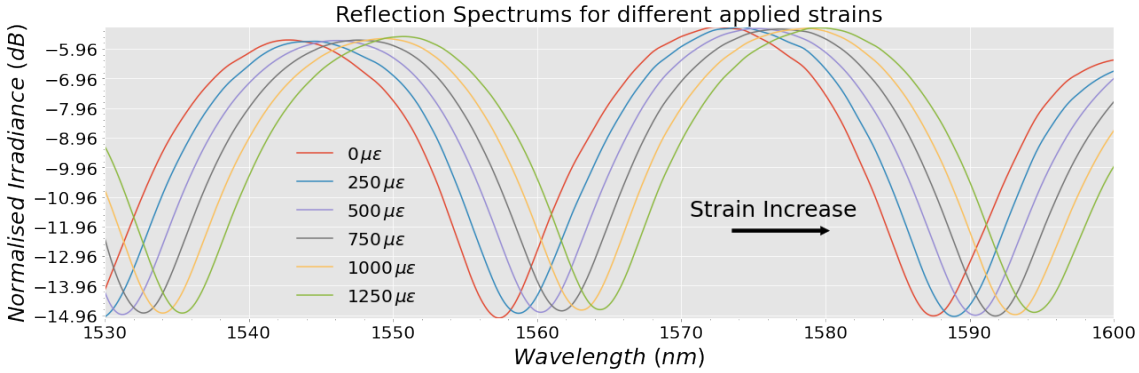

FIGURE 4.5: Optical spectrums of the FP cavity with length $L = 41.72\,\mu$m for several applied strains.

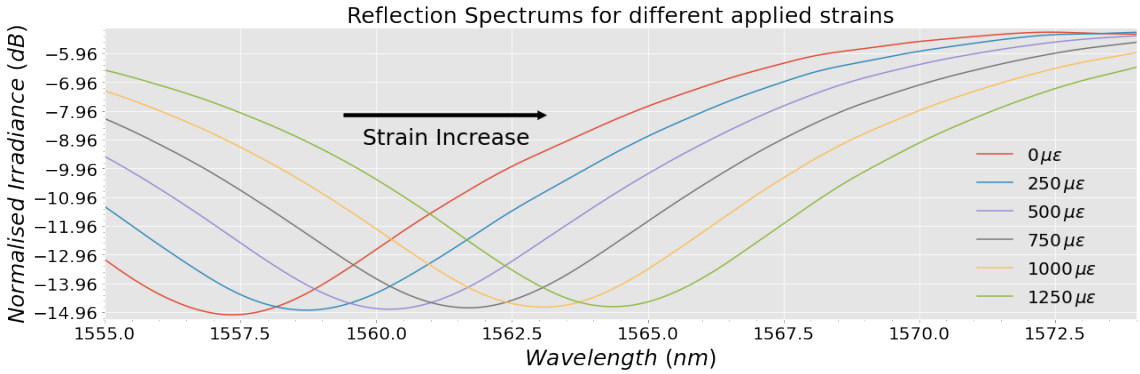

FIGURE 4.6: Redshift of the optical response. The peak shifts to longer wavelengths as the applied strain is increased.

As such, in order to quantify the shift of the wavelength induced by strain, one such peak was followed as the strain was increased. In the same way, the study was also

performed for a decrease in strain as the micro-translation stage was retorned to its initial position following a similar procedure to the loading process. By monitoring the reflected spectrum in the unloading process a blue shift was observed, *i.e.*, there was a shift of the signal to lower wavelengths. An identical analysis to the one described above was performed. It was found that the amount of red shift and blue shift were equal in absolute value. Therefore the sensitivities for the loading and unloading processes coincide, as seen in figure 4.8, thus allowing for repeatability.

To verify if the wavelength had any influence in the sensivity to strain a more detailed analysis was later performed where all the peaks were followed instead of only one. It was found that all the peaks were shifted by the same amount. As such, $\frac{d\lambda}{d\epsilon}$ is a constant parameter for a given FP sensor with fixed length.

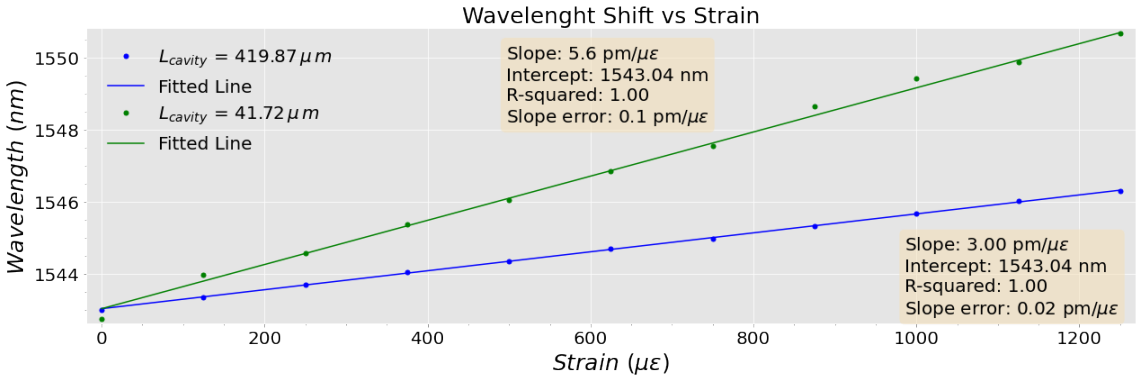

FIGURE 4.7: Plot of correlation of the wavelength shift and applied strain for two different cavities. The lengths of the cavities are $L_{small\,cavity} = 41.72\,\mu$m and $L_{big\,cavity} = 419.87\,\mu$m.

It is observed in figure 4.7 a linear correlation of the wavelength shift and the applied strain for two FP cavities with different lengths. One of the cavities had a very short length, namely $L_{cavity} = 41.72\,\mu$m while the other presented a bigger physical length, namely $L_{cavity} = 419.87\,\mu$m. Furthermore, a similar type of relationship is found for all the remaining FP cavities. It was found that the sensitivity, which is defined as the quotient of the change in the output signal and the change in the input signal, *i.e.*, $\frac{\partial\lambda}{\partial strain}$, for the two FP cavities differed. The sensitivity for the sensor with short length is estimated to be (5.6 ± 0.1) pm/$\mu\epsilon$ while the sensitivity for the longer sensor is estimated to be (3.00 ± 0.02) pm/$\mu\epsilon$, which are represented by the green dots in figure 4.8. Therefore, the sensivity of the sensor to strain varied as this analysis was conducted for all FP cavities, as seen in figure 4.8.

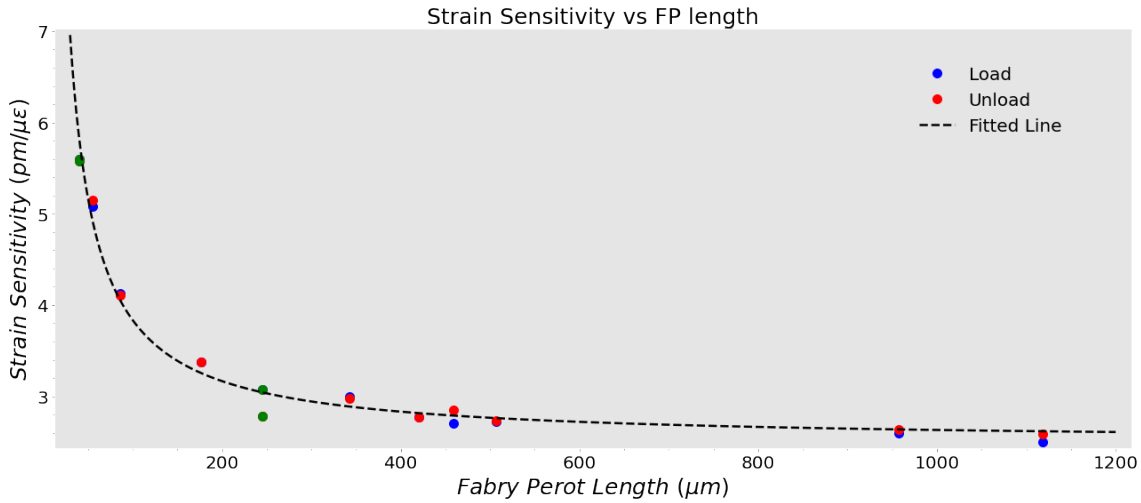

FIGURE 4.8: Relation between the strain sensitivity and the length of the FP cavities.

In the graphic above, a correlation between the sensitivity to strain and the length of the FP cavity is evident. The curve suggests that the relationship between the sensitivity to strain and the length of the FP interferometer is modeled by the following equation:

$$Strain_{sensitivity} = A + \frac{B}{FP_{length}} = 2.50 + \frac{133.82}{FP_{length}} \tag{4.2}$$

where A and B are coefficients.

The model of equation 4.2 can be verified by doing a linearisation of the data and representing the sensitivity as a function of the inverse of the FP length.

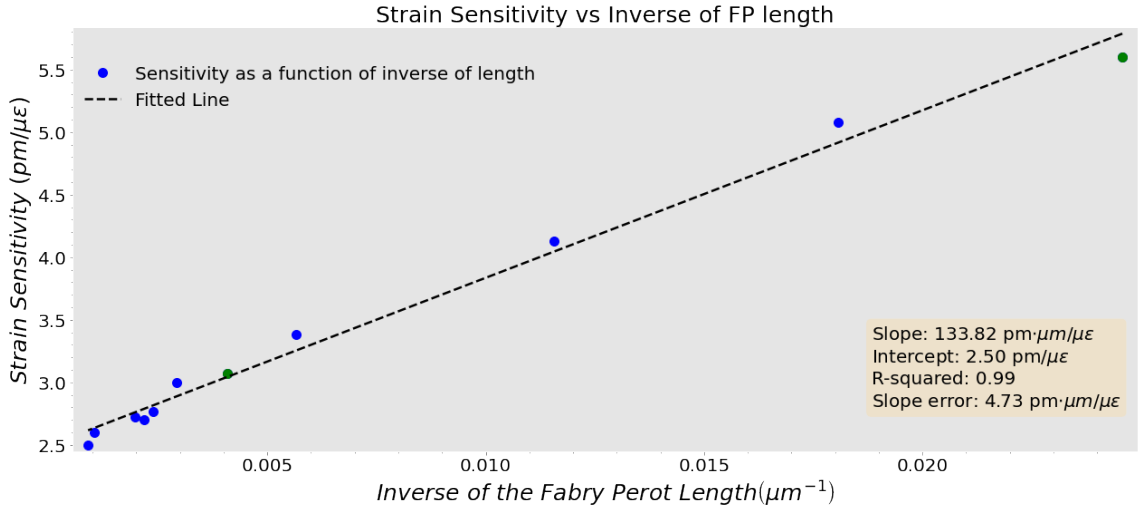

FIGURE 4.9: Relation between the strain sensitivity and the inverse of the FP cavity length. A linear correlation is observed proving that the model from equation 4.2 is valid.

Upon analysing the graphic from figure 4.9, it is concluded that a linear correlation

between the strain sensitivity and the inverse of the FP cavity length exists, with a coefficient of correlation (R-squared) of 0.99. Therefore, it is shown that equation 4.2 presents a good model to explain the relationship between the strain sensitivity and the FP length, with the coefficients A and B being respectively 2.50 $pm/\mu\epsilon$ and 133.82 $\mu m \cdot pm/\mu\epsilon$. By representing the sensitivity to strain in function of the inverse of the FP cavities length, it can be infered that the coefficient A can be regarded as the limit of the sensitivity to strain as the length of the FP cavity tends to increase to higher values, *i.e.*, the inverse of the FP cavity lenght tends to decrease to smaller values. Furthermore, the coefficient B can be associated with the rate of increase of the strain sensitivity with regards to the increase of the inverse of the FP cavity length.

As can be seen in equation 3.31, the phase term has a dependence on the length of the FP cavity. When the fibre is stretched, *i.e.*, an additional ΔL is applied to the sensor, the argument of the cosine is going to suffer a shift. Therefore, as seen in the graphic of figure 4.6 there is a red shift of the wavelengths for the loading process. As already seen this red shift is inversely proportional to the FP cavity length, *i.e.*, the variation of the optical length is greater in smaller sensors. As the length of the FP cavity is increased, the variation in optical length needed to shift the phase of the signal by 2π is lesser, *i.e.*, the phase necessary to shift the maximum to the neighbouring position. Therefore, the peaks of the reflected signal have an increasingly smaller red shift as the length is increased and the sensitivity diminishes. Similar findings were reported in the literature [47].

4.3.2 Temperature Characterization

A thermal caracterization of the sensors was also carried out. The sensor was placed in a Peltier cell, which is shown in figure 4.10 and an electric signal was applied to the terminals of the Peltier cell in the range $[0, 8]$ V. This caused a gradual increase of the temperature of the sensor in the range $[24, 90]^{o}$C. To control the temperature a digital thermometer was used. The response of the signal to the temperature increase was monitored with the scheme shown in figure 4.3.

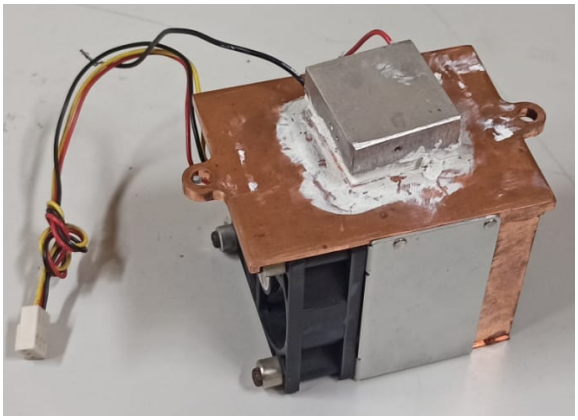

FIGURE 4.10: Peltier Cell used for the characterization.

In figure 4.11, a similar redshift to the one observed during the study of the response to strain was noticeable. However:

- The coefficient of volumetric thermal expansion of an ideal gas at constant pressure (α) is given by $\alpha = \frac{1}{T}$ [48]. So, α is of the order of $10^{-3}/^{o}C$ for the range of temperatures considered;
- The HCF is composed of air.

Therefore, the amount of redshift is substantially lower than the redshift observed during the strain study. This discrepancy is due to the small variation of the cosine argument compared to the lengths of the FP cavities since the cavities have lengths in the order of hundreds of micrometers. Furthermore, the effect of the increase of temperature will be similar between all FP cavities since the expansion of the HCF will be identical in each sensor. This result can be seen in figure 4.12 where the sensitivities are scattered around the mean value of the sensitivities of 0.85 $pm/^{o}C$ which is depicted as a red line in the figure.

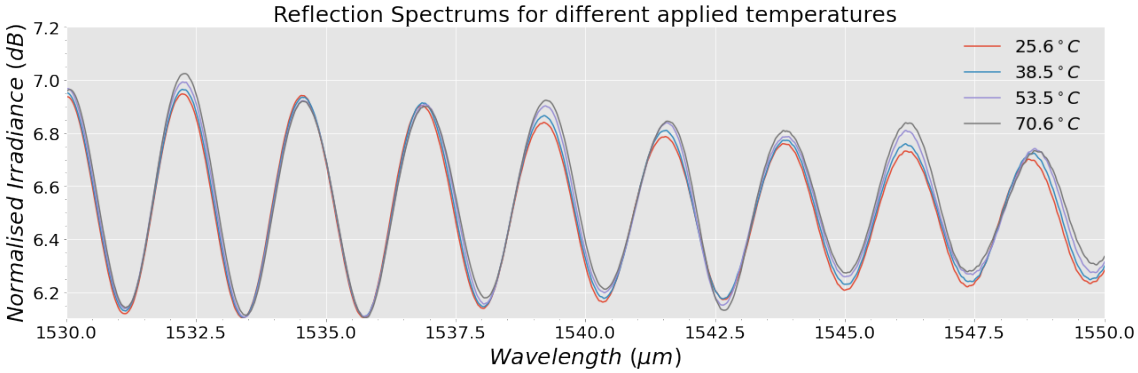

FIGURE 4.11: Redshift of the optical spectrum of the FP cavities for different values of temperature for a sensor with length $L = 478.38\,\mu m$.

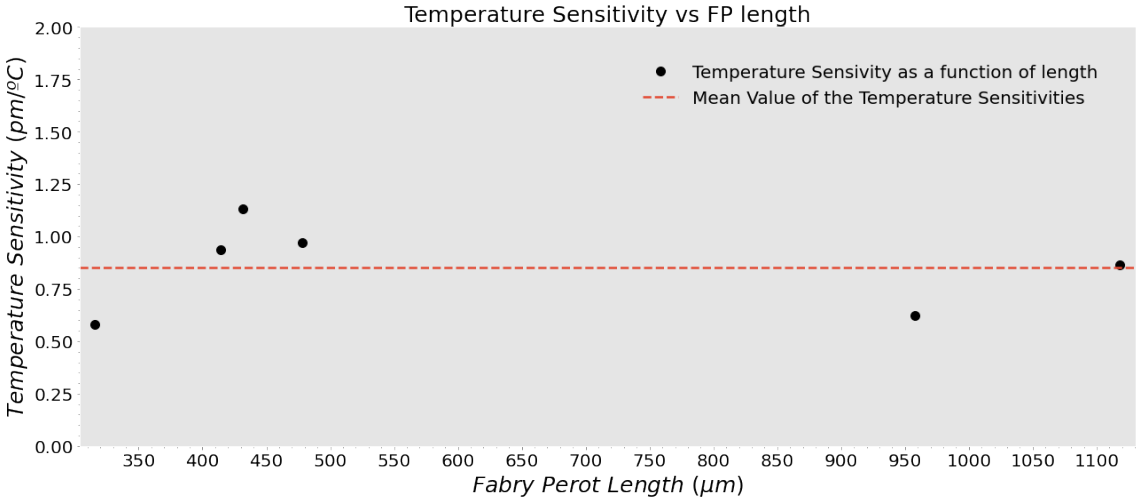

FIGURE 4.12: Relation between the temperature sensitivity and the length of the FP cavities.

The cross sensitivity was also calculated for the characterized sensors and the effect of temperature on strain can be determined, as the cross sensitivity, that is depicted in figure 4.13, is given by:

$$Cross\ Sensitivity = \frac{\frac{d\lambda}{d^{\circ}C}}{\frac{d\lambda}{d\mu\epsilon}} = \frac{d\mu\epsilon}{d^{\circ}C} \tag{4.3}$$

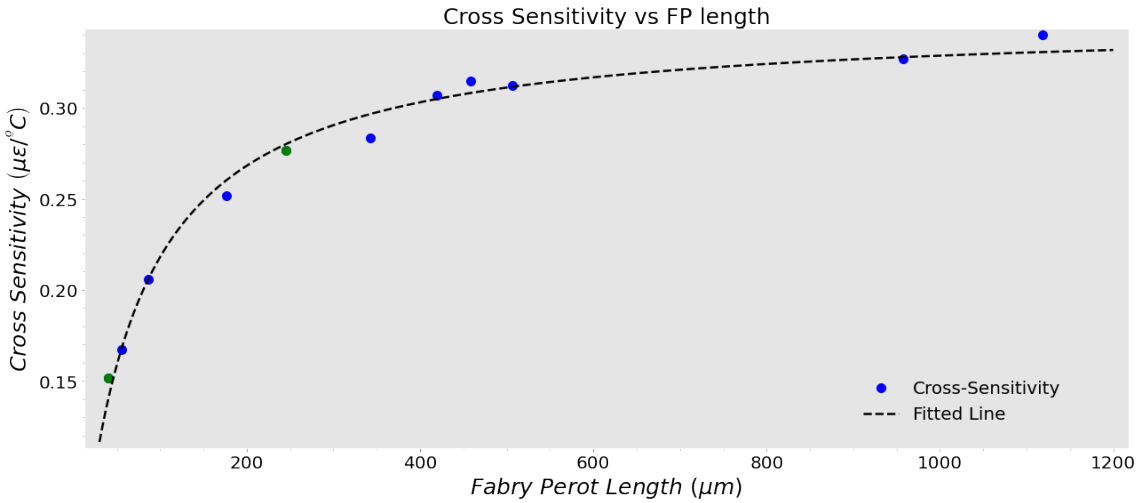

FIGURE 4.13: Relation between the cross sensitivity and the length of the FP cavities.

For cavities with longer length, the cross sensitivity is greater while for short cavities the effect of temperature on strain is not as significant. This implies that the determination of a given FP sensor produced with the process described here, for a specific location, needs to take into account the cross sensitivity and the strain sensitivity. As longer FP cavities exhibit a higher cross sensitivity they are not adequate to measure strain in environments with a temperature variation as strain is induced in the sensor by the thermal variation. However, if the temperature is stable these sensors could prove advantageous since longer FP cavities are easier to produce. On the other hand, if the application demands a more sensitive sensor a FP cavity with a short length should be used. Although short FP cavities are more difficult to manufacture the low cross sensitivity enables the use of these short sensors in areas where there is thermal variation, *i.e.*, there is no control of the temperature.

4.4 Concluding remarks

In this chapter it was concluded that the lenght of a FP cavity influences the sensitivity to applied strain and the relation between those two quantities is reged by equation 4.2. Hence, shorter cavities present the highest sensitivity and longer cavities are less sensitive. As such, the behaviour of low-finesse FP sensors is better understood and these results could prove useful in determining the length of the cavity needed for the application in question. On the other hand, the results of the thermal caracterization that was carried out demonstrated that the sensitivity of the FP sensors to temperature remains

pratically constant for the range of temperatures used. The results also imply that the FP cavities exhibit low sensitivity to temperature and are in agreement with the findings of [49]. Furthermore, it was determined that the cross sensitivity goes from 0.10 to 0.35 as the length of the cavity is increased. Hence, cavities with smaller length could be more suitable in applications where there is a significant variation of temperature.

Chapter 5

Development and Characterization of Optical Interrogation System

5.1 Introduction

In this chapter a simple interrogation system is developed and characterized. First, the optical interrogator scheme is explained. Afterwards, the optical interrogator is subjected to two characterizations in two different domains. Considering the importance of the LIRA project there was a need to characterize the optical interrogation system in order to understand its limitations, ascertain the operation conditions of the aforementioned system and discover if it fulfilled the requirements established for the project. Finally, the interrogation system was used to monitor the shift of the cross correlation signal as external parameters are applied namely displacement and strain.

5.2 Optical System

5.2.1 Characterization in Amplitude

In figure 5.1, a scheme of the experimental setup is presented. It is composed of a Superluminescent Light Diode commercial broadband light source, a four port circulator, a Thorlabs PK4GA7P1 linear piezoelectric stack (PZT), a Hewlett Packard 33120A commercial function generator, a TEGAM Model 2350 high voltage amplifier, two Fabry Perot (FP) cavities and a Yokogawa AQ6370C Optical Spectrum Analyser (OSA). The broadband source has a bandwidth of 90 nm with a center wavelength of 1550 nm. In this figure the used PZT is also shown.

The interrogation system was composed by a FP cavity which has a PZT attached to one of its reflective surfaces. The reflective surfaces of this interrogator cavity are the cleaved end of a single mode fibre (SMF) and a highly reflective mirror. Therefore this cavity is in air. The SMF was placed on a fibre clamp. The fibre clamp itself was attached to a micro-translation stage. Thus, the equilibrium length of the FP interrogator could be estimated. The system was used to interrogate the second FP cavity that was acting as a sensor and whose length is $L = 191$ μm. The commercial function generator applied a electric signal to the PZT in order to dynamically and mechanically alter the physical length of the FP interrogator cavity. Before being applied to the PZT, the electric signal was amplified by the high voltage amplifier with an amplification factor of 50. The interrogation system was designed to have a variation of the order of micrometers. Therefore, it was essential that the lengths of the two FP cavities were similar. Hence, the control of the length of the static FP cavity was important. The cavity that was emulating a sensor was manufactured using the same setup from chapter 4, *i.e.*, the scheme shown in figure 4.1.

Finally, the optical beat between the two signals, which was derived in Appendix B was detected at the OSA. Thus, the interrogation system could be characterized and its behaviour could be better understood.

Initially, the amplitude of the electric signal applied to the PZT was varied while the frequency of the signal was fixed. After this characterization the roles were inverted and the frequency was changed while the amplitude remained constant. A triangular signal was used in order to perform the characterization in amplitude as well as in frequency. The signal chosen had this shape to assure that the rate of change of the cavity length was constant.

The amplitude of the electric signal applied to the PZT was varied in the range $[0.50, 2.50] \pm 0.01$ V with a fixed frequency of 5.0 ± 0.1 Hz. Due to the operating conditions of the PZT a DC offset was added to each AC electric signal in order to ensure that no negative voltage was present in the signal. Therefore the value of the DC offset was dependent on the value of the amplitude.

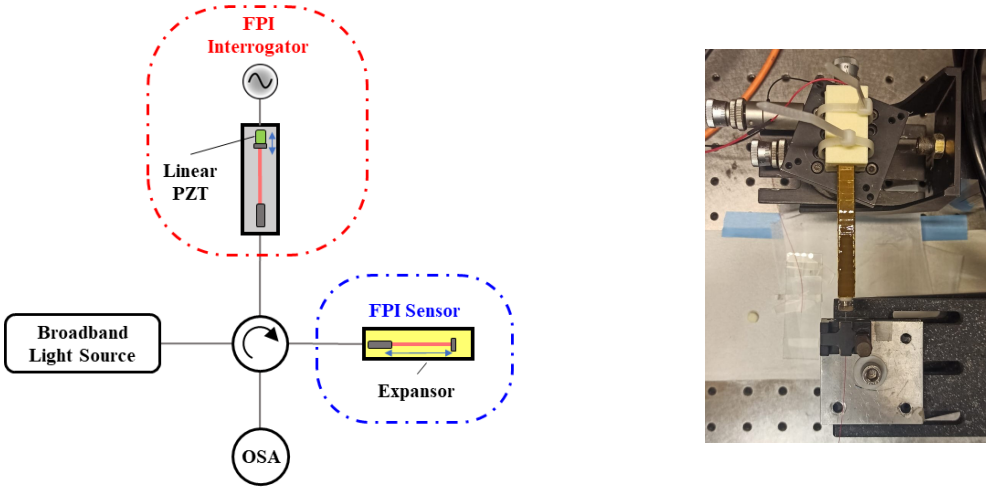

FIGURE 5.1: Scheme of the setup and a FP interrogator consisting of a in-air cavity. The reflective surfaces of the FP are the end face of a SMF and a mirror coupled to a PZT.

In figures 5.2 and 5.3 the optical beat between two signals, each coming from a different FP cavity, *i.e.*, equation 3.31, for different applied amplitudes, namely (0.50 ± 0.01) and (2.50 ± 0.01) V is observed. Due to the dinamic variation of the PZT the resultant signal is given by equation 3.42, where $\phi_1 = 2\beta L_1$ and L_1 is a function of time.

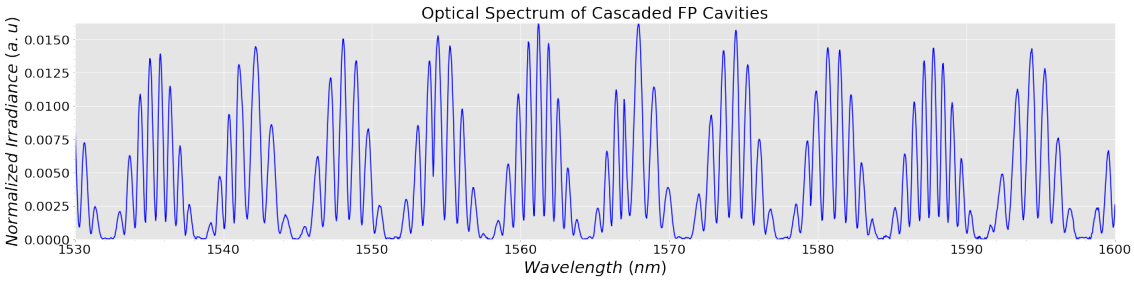

FIGURE 5.2: Optical Spectrum of two cascaded FP cavities for a amplitude of the electric signal of (0.50 ± 0.01) V.

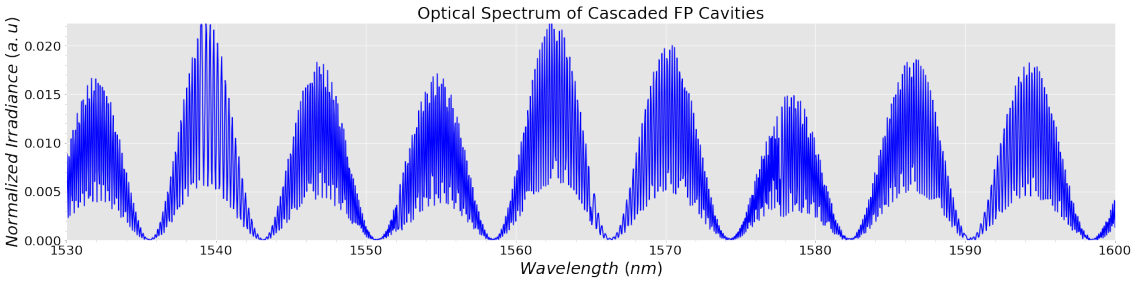

FIGURE 5.3: Optical Spectrum of two cascaded FP cavities for a amplitude of the electric signal of (2.50 ± 0.01) V.

Since the OSA has a low response time it is not able to accompany the variation of the phase of the signal as it is being detected. Nonetheless, an optical beat is still observed in figures 5.2 and 5.3 as the lengths of the two FP cavities always remain similar. Therefore the frequencies of the two cosine signals are always close to one another.

5.2.2 Characterization in Frequency

For this work, the setup used was the same setup presented in figure 5.1 and described in section 5.2.1.

As seen in figure 5.4 the signal which corresponds to the beat phenomenon is modulated. This modulation arises because the PZT is actively and rapidly changing the FP cavity length. For low frequencies the length variation is slow. Therefore, as already stated, a signal which has the shape of a beat between the two signals from the two cavities is observed. On the other hand, as the frequency is increased the OSA is limited in detecting the fast change of cosine signals which contain the term L_1. Hence the beat between the two signals is absent in figures 5.5 and 5.6. What is observed is a small modulation of a simple cosine signal, *i.e.*, the signal of the static sensor, more concretely cos $(2\beta L)$ that still arises from the swift change in length of the PZT. Furthermore, as the frequency is gradually increased the modulation disappears alltogether and the only contribution from the interrogator cavity to the optical spectrum of two FP cavities in series is the mean value of the fast changing signal, as depicted in figure 5.6.

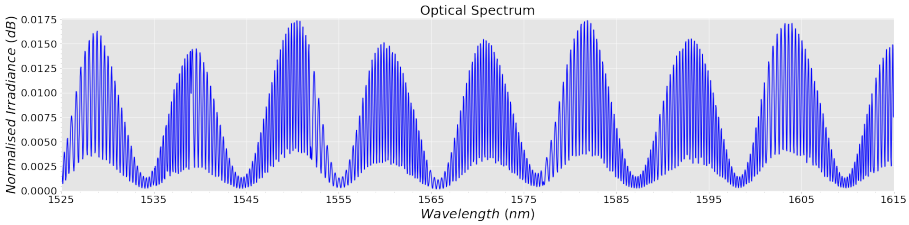

FIGURE 5.4: Spectrum of the cross correlation for a applied frequency of (0.5 ± 0.1) Hz.

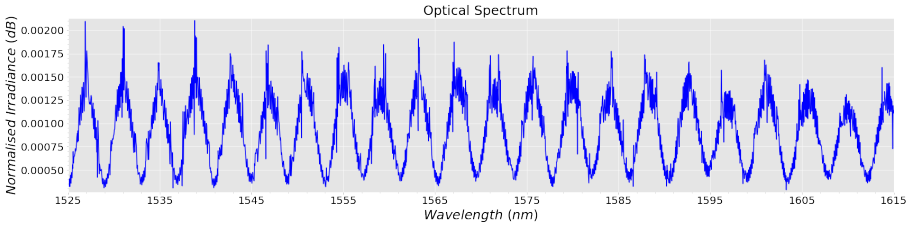

FIGURE 5.5: Spectrum of the cross correlation for a applied frequency of (5.0 ± 0.1) Hz

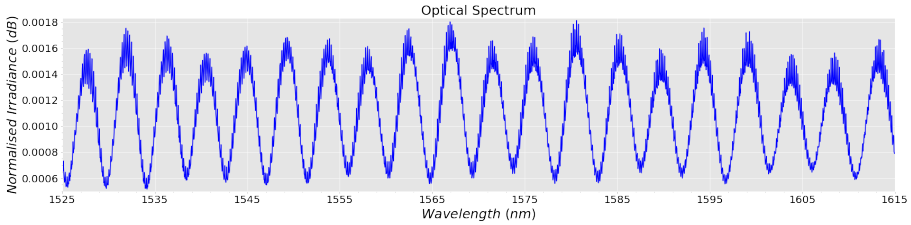

FIGURE 5.6: Spectrum of the cross correlation for an applied frequency of (65.0 ± 0.1) Hz

5.3 Optoeletronic System

5.3.1 Characterization in Amplitude

In the prior section it was verified that the detection system was limited in the detection of the fast changing signal and failed in capturing all the information about the system. Thus, a detection system which was capable of detecting the swift change of the signal was needed. Therefore the experimental setup used for the remainder of the work is quite similar to the one that was used in section 5.2, as can be seen in figure 5.7. The only difference between the two setups is that for the work carried out henceforth the detector utilized is no longer an OSA but a ThorLabs PDA10CS-EC InGaAs Amplified Photodetector which is connected to an GWINSTEK GDS-2304A oscilloscope. To retrieve the desired signal from this measuring instrument a Python Script was developed that enabled the communication between the oscilloscope and a personal computer. This script is presented in Appendix D.

A similar characterization to the one done above was then performed to assess the behaviour of the cross correlation between the two signals of each FP cavity. As before, the PZT was driven by a triangular signal. The reason behind the choice for the triangular signal remains the same. Initially, the response of the system was monitored as the amplitude of the electric signal was increased while the frequency was kept constant. Since that in the range of voltages applied to the PZT the length of the cavity has a linear correlation with the amplitude of the electric signal applied, as seen in figure E.1, a greater applied amplitude corresponds to a greater range of lengths swept by the FP interrogator. Afterwards, the roles were reversed and the frequency was varied as the amplitude of the electric signal was unaltered.

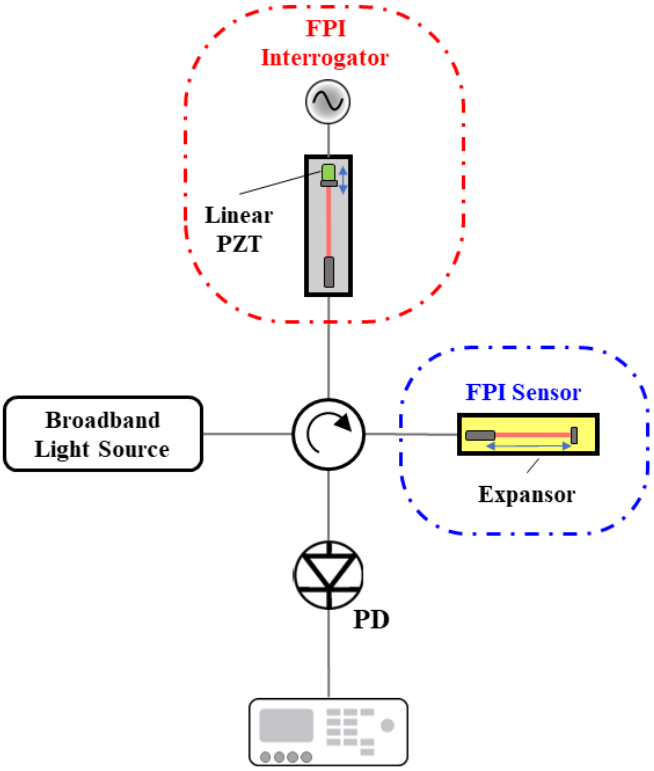

FIGURE 5.7: Scheme of the experimental setup used for the characterization of the optoeletronic signal.

The triangular signal had a frequency of (5.0 ± 0.1) Hz while the amplitude was varied in the range $[0.50, 2.00] \pm 0.01$ V. Due to the amplification factor of the high voltage amplifier the applied amplitude to the PZT was in the range $[25.0, 100.0] \pm 0.5$ V. The FP cavity length, *i.e.*, 200 μm, is then driven from its equilibrium position to increasingly smaller lengths, since the PZT diminishes the FP cavity length while the electric signal increases in amplitude.

The variation of the applied amplitude can be seen in figure 5.8 a). In figure 5.8 b) the optoeletronic response is observed. This signal has a sinc envelope modulated by a fast changing signal as predicted by equation 3.46. Thus it was shown that the optical interrogation system was functional.

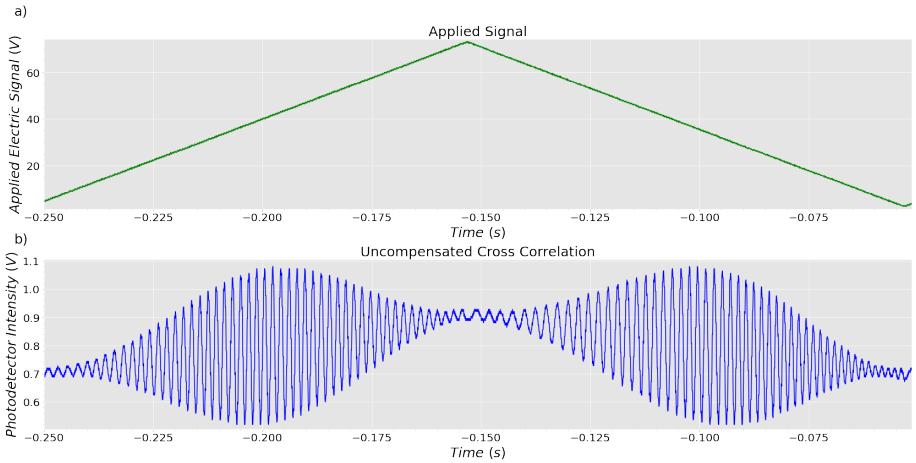

FIGURE 5.8: Cross-correlation for a applied amplitude of (70.00 ± 0.50) V

Since two cicles of the cross correlation signal are present in figure 5.8, a single cicle to better illustrate the time behaviour of the cross-correlation signal is selected and presented below in figure 5.9. As predicted by equation 3.46 the maximum corresponds to the time instant where the two cavities have the same optical length. Therefore, in that time instant both cavities have identical physical lengths, considering that the refractive index is equal in both cases, *i.e.*, $n = 1$. Due to this property, the length of the FP cavity acting as a sensor can be demodulated if the length of the FP interrogator is known.

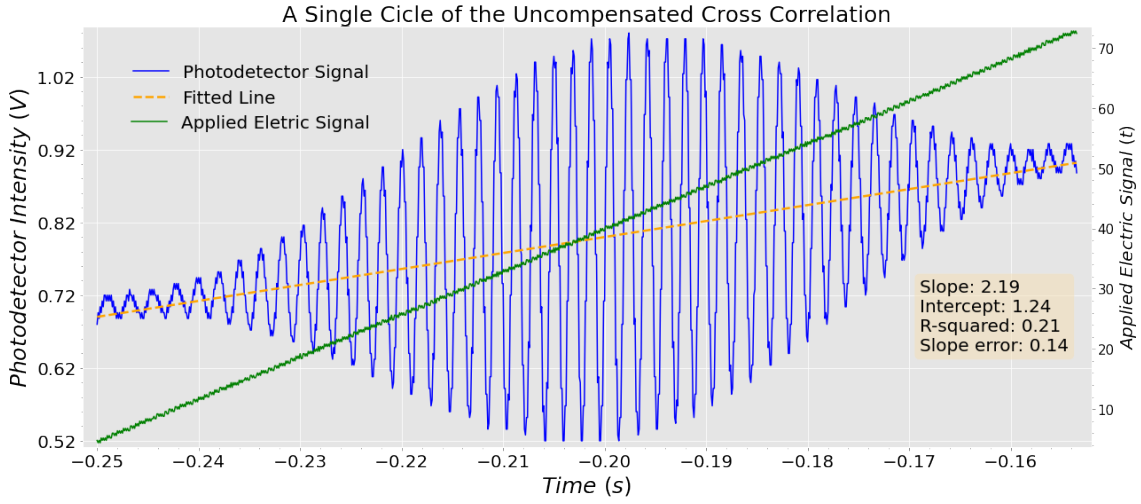

FIGURE 5.9: A single cicle of the cross-correlation for a applied amplitude of (70.00 ± 0.50) V

Furthermore, and more importantly, if a small change of the FP cavity acting as a sensor happens the time instant of the maximum of the cross correlation is shifted, *i.e.*, there is a phase shift in the argument of the cosine signals which are a function of the variable L. This phase shift is the root of this time shift since now the two signals from

each FP cavity are in phase at another optical length. Because of this time shift it is possible to track when a external physical parameter induces a change in the optical path lenght of the FP sensor. By monitoring the position of the maximum, the effect of the physical parameter on the optoeletronic signal can be measured.

Furthermore, the detection system of this interrogator, *i.e.*, the photodetector, has a response time which is only limited by the speed of the electrons [50] and then has a faster detection speed than a traditional OSA. Hence the detection system is capable of measuring fast changes of the signal. Additionally through the use of a oscilloscope a greater resolution is achieved. Therefore the interrogation system developed is suitable to be used in applications where there is the need to measure dynamic signals or small variations of the physical parameter.

However a small tilt is observed. This tilt is due to geometrical losses that are present when the light propagates in the air from the fibre end to the mirror and back. Which means that the light that is recoupled in the SMF has less power than the light that was initially decoupled from the fibre. This effect is undesirable as tracking the peak of the cross correlation signal becomes more challenging. To remove this effect a linear fit was adjusted to the signal, as seen in figure 5.9. Afterwards the slope of the regression line was subtracted to the data, as presented in figure 5.10.

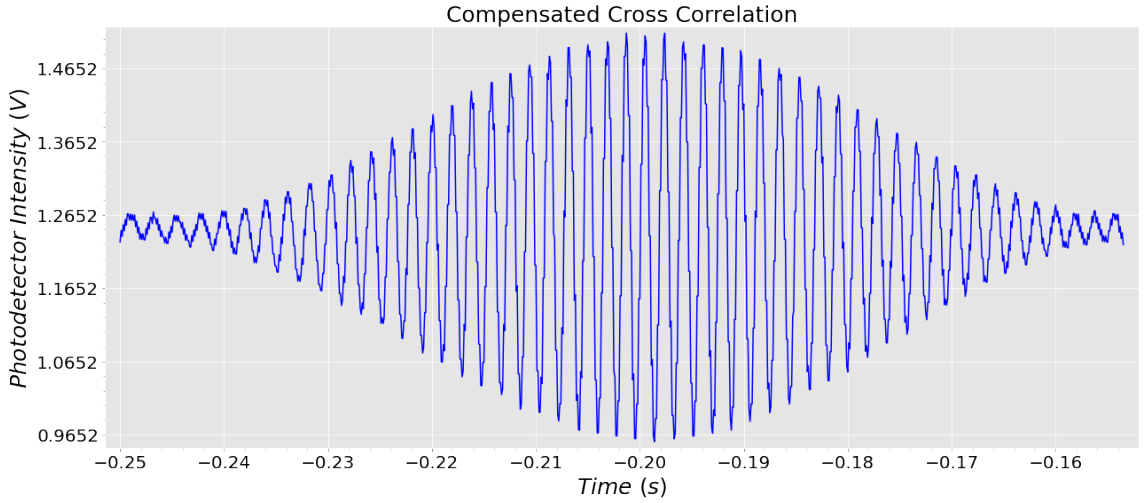

FIGURE 5.10: Compensated cross-correlation for a applied amplitude of (70.00 ± 0.50) V

Now that the signal is compensated, it is possible to better accompany the time shift of the maximum.

5.3.2 Characterization in Frequency

The frequency characterization was performed with the setup pictured in figure 5.7. In this work the amplitude of the applied electric signal was kept constant throughout it and its frequency was varied in the range $[0.5, 100.0] \pm 0.1$ Hz. A study of the stability of the cross correlation signal was done as the frequency was increased. The system presented good stability throughout the characterization, as can be seen in figure 5.11, where the sinc signal predicted by equation 3.46 is visible for a frequency of the applied electric signal of (25.0 ± 0.1) Hz.

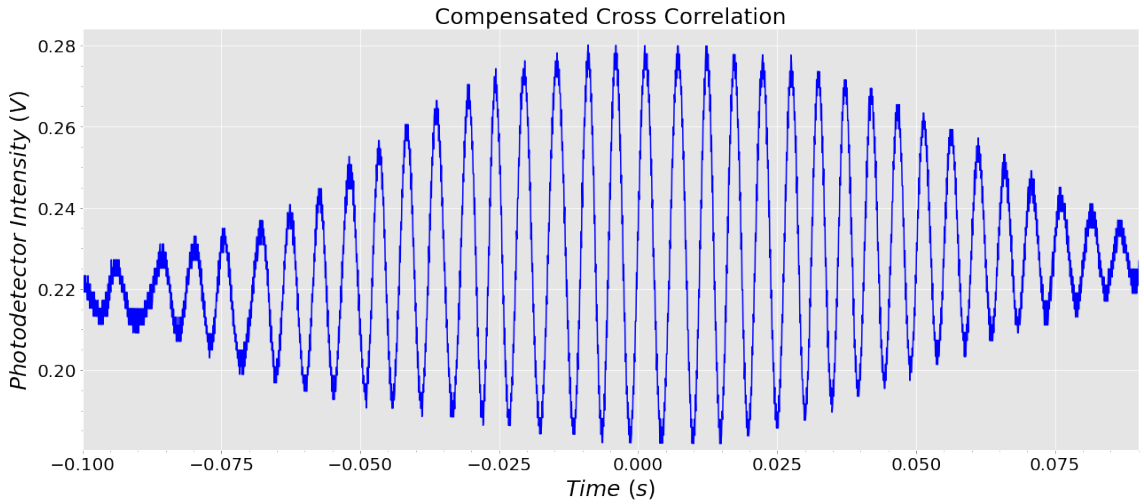

FIGURE 5.11: Cross correlation for a applied frequency of (25.0 ± 0.1) Hz

5.4 Measurements of Physical Parameters

After the development of the interrogation system the same was used to measure with absolute precision physical parameters. The shift of the cross correlation signal was monitored as the length of the FP interrogator cavity was decreased by means of the micro-translation stage. The length of the static FP cavity was unaltered. Furthermore, the optical interrogation system was subsequently used to measure the strain that was induced in the static FP cavity. The maximum of the cross correlation signal happens when the cavities are balanced, *i.e.*, are in phase. Therefore, since both FP cavities are identical apart from the length, *i.e*, are composed of an air gap and hence have $n = 1$, the cavities are in phase when the FP interrogator is of the same length of the FP sensor. When the physical length of the FP sensor is changed the time instant of the maximum is subjected to a shift.

5.4.1 Displacement Measurement

The optical interrogation system was utilized as a displacement sensor. The two reflective surfaces of the interrogator cavity were approached by means of a micro-translation stage while the FP sensor remained fixed. This is similar to altering the length of the FP sensor and keeping the equilibrium length of the FP interrogator unaltered. The cavity was displaced to a maximum of (5.0 ± 0.5) μm in steps of (1.0 ± 0.5) μm. Additionally the PZT was driven by a electric signal with a frequency of (9.0 ± 0.1) Hz and an amplitude of (105.00 ± 0.50) V with an offset of (10.000 ± 0.005) V. As the FP interrogator length was decreased a time shift of the envelope to the left was verified, as seen in figure 5.12. A linear relation between the induced displacement and the time shift of the maximum is observed in figure 5.13. A sensitivity of (-5.84 ± 0.52) ms/μm is reported.

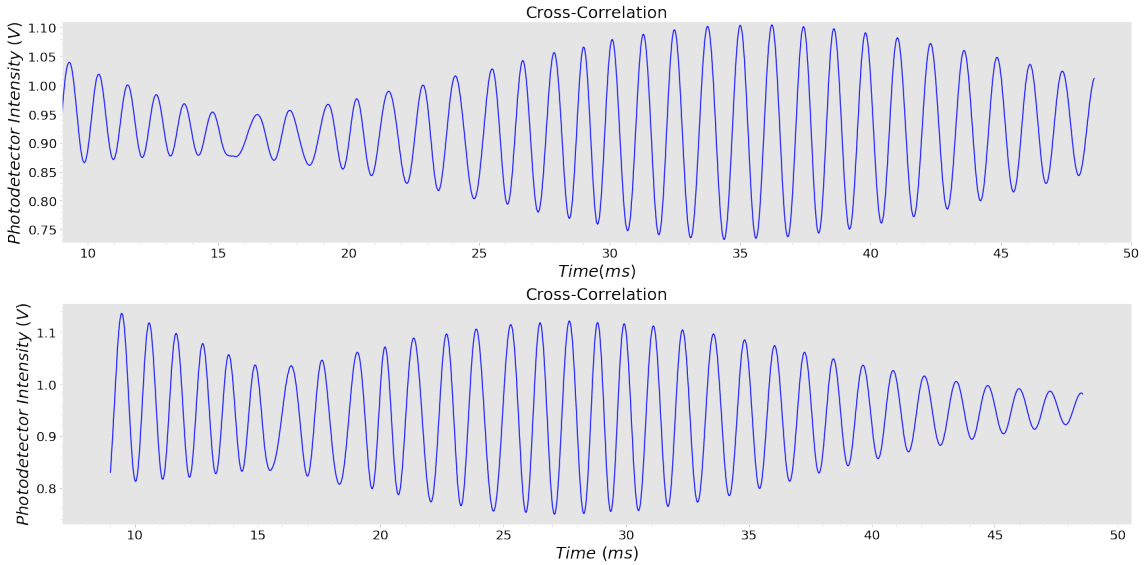

FIGURE 5.12: Time shift of the cross-correlation signal caused by a change of the equilibrium length of the FP interrogator.

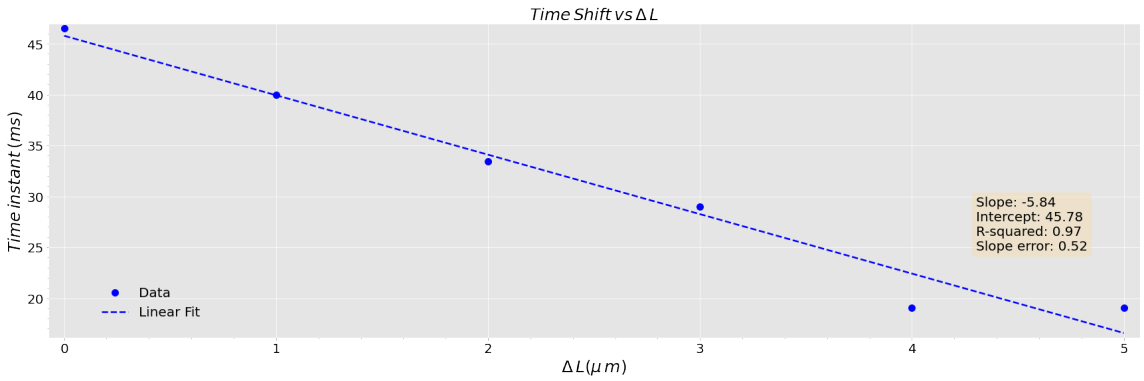

FIGURE 5.13: Relation between the time shift and the change in the length of the FP interrogator.

5.4.2 Strain Measurement

One portion of the in-fibre FP cavity was fixed with adhesive to a linear translation stage while another was fixed to a platform. The length of the FP cavity was changed to induce strain on the sensor. Additionally an electric signal with a fixed frequency of (15.0 ± 0.1) Hz and a fixed amplitude of (50.00 ± 0.50) V with an offset of (30.000 ± 0.005) V was applied to the PZT. Hence the PZT continuously varied the length of the FP interrogator.

The time response was monitored on the oscilloscope, as seen in figure 5.14. A shift of the envelope was observed. The maximum peak of the sinc envelope was tracked. As the FP cavity is stretched the length of the FP sensor approaches the equilibrium length of the FP interrogator. Therefore, as strain is increased, the two FP cavities had identical physical lengths at an earlier time instant and the envelope shifted to the left.

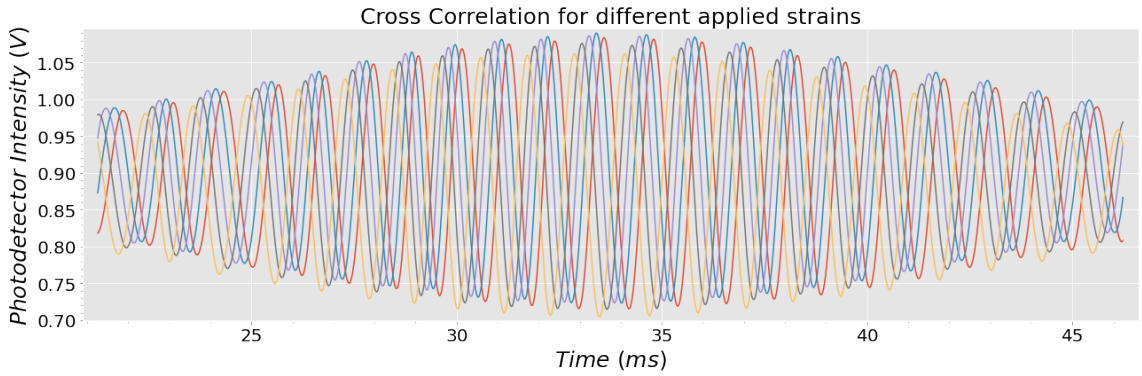

FIGURE 5.14: Cross-correlation signal for different values of applied strain. A time shift of the signal is observed.

To better observe the shift a zoom in the range $[32.6, 33.8]$ ms is performed and is presented in figure 5.15.

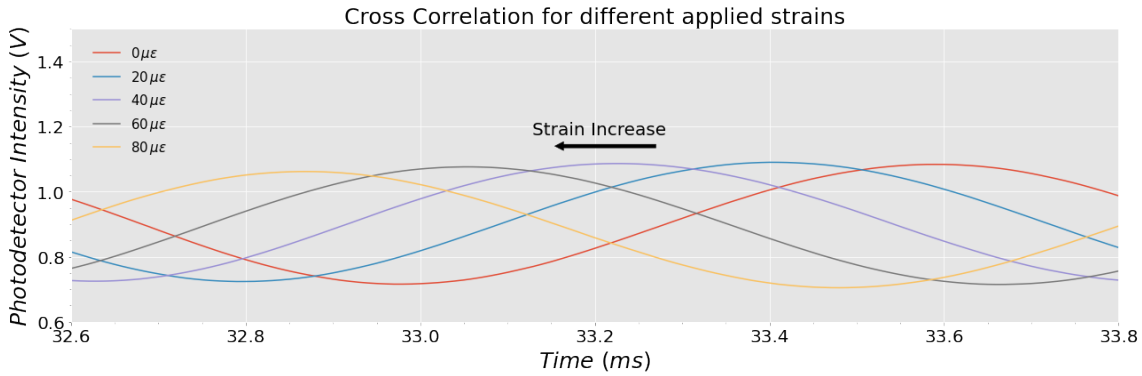

FIGURE 5.15: Cross-correlation signal for different values of applied strain. A time shift of the signal is observed.

As observed in figure 5.16, the time shift of the maximum presents a linear correlation with the applied strain. It was found that the sensitivity for the envelope shift is $(-8.82 \pm 0.12)\,\mu s/\mu\epsilon$.

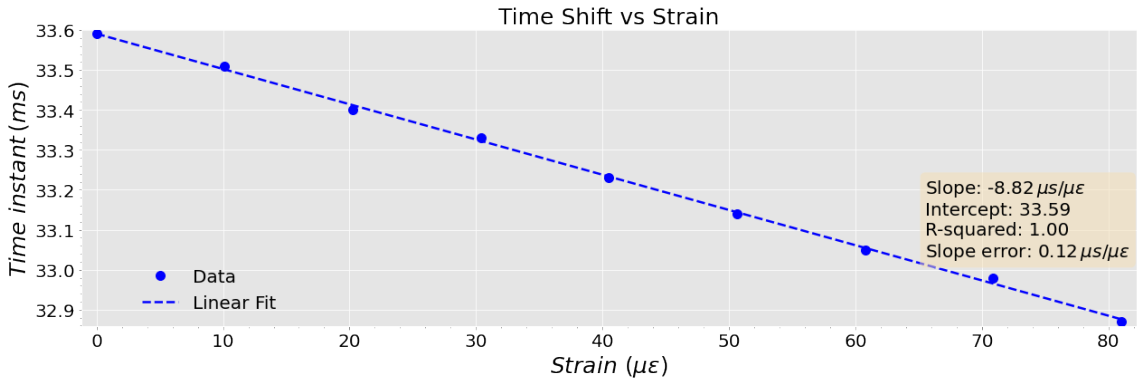

FIGURE 5.16: Relation between the time shift and the applied strain to the FP sensor.

5.5 Concluding Remarks

A optical interrogation system was developed and characterized. The results show that the optical beat between two signals disappears for frequencies above (5.0 ± 0.1) Hz and is unable to accompany the swift variation of the PZT. Therefore we showed that this system has limitations. To overcome these limitations the detection system was changed to a photodetector and the cross correlation was displayed on an oscilloscope. The stability of the cross correlation was examined. It was found that the signal remained stable for a larger range of frequencies. In addition, the signal remained stable throughout the amplitude characterization. Hence, we concluded that the interrogation system was operational. In the end, the interrogation system was used and it was comproved that by changing the optical length of the second interferometer and thus inducing strain, a shift of the maximum is observed. The sensitivity was estimated to be $(-8.82 \pm 0.12)\,\mu s/\mu\epsilon$. Furthermore, a displacement study was also carried out. The equilibrium length of the FP interrogator was shifted by means of a micro-translation stage. The sensitivity was estimated to be (-5.84 ± 0.52) ms$/\mu m$.

Summarising the parameters for the displacement study and strain study are repeated in tables 5.1 and 5.2, respectively.

TABLE 5.1: Applied Signal and Optoeletronic Signal Parameters for the displacement study

Parameters	**Values**
Initial Amplitude	(2.10 ± 0.01) V
Frequency	(9.0 ± 0.1) Hz
Amplification Factor	50
Amplified Amplitude	(105 ± 0.50) V
Applied Offset	(10.000 ± 0.005) V
Range of Sweep	$(0 - 78)$ μm
Applied Displacement	$(0.0 - 5.0)$ μm
Sensitivity	(-5.84 ± 0.52) ms/μm

TABLE 5.2: Applied Signal and Optoeletronic Signal Parameters for the strain study

Parameters	**Values**
Initial Amplitude	(1.0 ± 0.1) V
Frequency	(15.0 ± 0.1) Hz
Amplification Factor	50
Amplified Amplitude	(50 ± 0.50) V
Range of Sweep	$(0 - 40)$ μm
Applied Strain	$(0 - 80)$ $\mu\epsilon$
Sensitivity	(-8.82 ± 0.12) μs/$\mu\epsilon$

Chapter 6

Conclusions and Future Work

The first three chapters present an overview that includes fibre optic sensors, interrogation systems and some theoretical concepts. The other two chapters include the experimental part of Fabry Perot (FP) sensors and an interrogation system. Regarding the last chapter, perspectives for improving the work carried out within the scope of this thesis are also discussed.

In chapter 1 the objectives of the thesis were established. Additionally, the motivation and the outputs of this dissertation were introduced.

In chapter 2 a historical perspective of the uses of FP sensors was presented. Some previous studies carried out with FP cavities were mentioned and debated. Furthermore the importance of optical interrogation systems was emphasised as several novel interrogators were listed and explained.

In chapter 3 the fundamental theory behind this work was introduced. The key equations were listed. Afterwards they were represented in graphical form and the graphics were analysed and explained.

In chapter 4 the process of fabricating FP cavities was presented. All FP cavities had a length in the range $[30, 1200]\,\mu m$. Furthermore, a characterization of all FP sensors in regards to strain and temperature was discussed. It was found that the sensitivity to temperature was similar for all FP cavities characterized. It was reported that the average temperature sensitivity was $0.85\,pm/\mu\epsilon$. On the contrary, it was found that the length of the FP cavity had a influence on the FP sensor sensitivity to strain. It was concluded that FP cavities with longer length exhibited a lower sensitivity than longer FP cavities. The maximum and minimum sensitivities reported were, respectively, $(5.6 \pm 0.1)\ nm/\mu\epsilon$ and $(2.50 \pm 0.02)\ nm/\mu\epsilon$. The cross-sensitivity was also estimated and it was determined

that longer cavities presented a higher cross-sensitivity than cavities with shorter length. The cross-sensitivity varied in the range $[0.10, 0.35]$ $\mu\epsilon/^{\circ}C$. Thus, the study realized could prove useful in determining the FP cavity ideal for a necessary application.

However this study was carried out for ambient temperature, and there was no control of unwanted external parameters. Therefore, a way to improve this study could be recreating the study under different experimental conditions. The strain study could be performed for different temperatures to verify if the temperature has any effect on the strain sensitivity. Furthermore the range of applied strain could be extended to investigate if the wavelength shift and the applied strain still maintained a linear correlation.

In the temperature study the range of temperatures could also be extended, more concretely to hundreds of ºC. Hence, the effect of higher temperatures on the sensitivity to temperature could be investigated. The thermal stability of the optical signal could also be investigated. Furthermore the same study done in the scope of this thesis could be recreated for other type of FP cavities than the ones utilized throughout this thesis. In that way the influence of different types of FP cavities on the sensitivities to strain and temperature could be infered.

Regarding chapter 5, a simple interrogation system based on two cascaded FP cavities is reported. Due to the importance of the LIRA project the optical and optoeletronic responses of the interrogation system were characterized. It was confirmed that an Optical Spectrum Analyser (OSA) is unable to track the beat signal for frequencies of the electric signal applied to the PZT higher than (5.0 ± 0.1) Hz. Therefore the OSA was replaced by a high speed photodetector. Afterwards, it was verified that the optoeletronic signal had good stability for a higher range of frequencies, *i.e.*, $[0.0, 25.0] \pm 0.1$ Hz. Additionally, the signal also kept stable for all the amplitudes of the electric field applied in the range $[0.50, 2.00] \pm 0.01$ V. Thus it was comproved that the optical interrogation system was operational.

In the end the optical interrogation system was used. Two different studies were realized, more concretely, a displacement study and a strain study. The first study consisted in changing the equilibrium length of the FP interrogator and monitoring the cross correlation signal. A large shift of the signal was observed. It was reported that the shift was linearly correlated with the applied displacement and a sensitivity of (-5.84 ± 0.52) ms$/\mu m$ was estimated. In the second study the FP sensor cavity was fixed with adhesive to a micro-translation stage. Afterwards strain was induced in the sensor. It was found

that the shift of the time instant of the peak of the cross correlation and the applied strain were linearly correlated. A sensitivity of $(-8.82 \pm 0.12)\ \mu s/\mu\epsilon$ was reported.

However the work carried out during this thesis in the scope of the LIRA project was a small part of the work that is needed as this is an ongoing project. In the future the FP interrogator will be replaced by a in-fibre Mach Zender interferometer. Furthermore, the system needs to be optimized in order to achieve a μK resolution.

Appendix A

Derivation of the reflected irradiance of a in-fibre Fabry Perot cavity

The final reflected electric field of a in-fibre Fabry Perot (FP) cavity is repeated here:

$$\overrightarrow{E_{out}} = A \cdot \left(\overrightarrow{E_{in_p}} - \overrightarrow{E_{in_s}}\right) - B \cdot e^{i\phi} \cdot \left(\overrightarrow{E_{in_p}} - \overrightarrow{E_{in_s}}\right) \tag{A.1}$$

Since the irradiance is given by:

$$I = \overrightarrow{E} \cdot \overrightarrow{E^*} \tag{A.2}$$

the reflected irradiance is expressed by:

$$I_R = \overrightarrow{E_{out}} \cdot \overrightarrow{E^*_{out}} \tag{A.3}$$

Substituting equation A.2 in equation A.3, the resulting expression is:

$$I_R = \left[A \cdot \left(\overrightarrow{E_{in_p}} - \overrightarrow{E_{in_s}}\right) - B \cdot e^{i\phi} \cdot \left(\overrightarrow{E_{in_p}} - \overrightarrow{E_{in_s}}\right)\right] \cdot \left[A \cdot \left(\overrightarrow{E^*_{in_p}} - \overrightarrow{E_{in_s}}^*\right) - B \cdot e^{-i\phi} \cdot \left(\overrightarrow{E^*_{in_p}} - \overrightarrow{E_{in_s}}^*\right)\right] \tag{A.4}$$

Upon doing the multiplications in equation A.4 the following equation is obtained:

$$I_R = \left(A^2 - A \cdot B \cdot e^{-i\phi} - A \cdot B \cdot e^{i\phi} + B^2 \cdot e^{i\phi - i\phi}\right) \cdot \left[\left(\overrightarrow{E_{in_p}} - \overrightarrow{E_{in_s}}\right) \cdot \left(\overrightarrow{E^*_{in_p}} - \overrightarrow{E_{in_s}}^*\right)\right] \tag{A.5}$$

By noting that $e^{i\phi} + e^{-i\phi} = 2 \cdot \cos(\phi)$ and that $e^0 = 1$, the following equation is obtained:

$$I_R = \left(A^2 - 2 \cdot A \cdot B \cdot \cos(\phi) + B^2\right) \cdot \left[\left(\overrightarrow{E_{in_p}} - \overrightarrow{E_{in_s}}\right) \cdot \left(\overrightarrow{E^*_{in_p}} - \overrightarrow{E_{in_s}}^*\right)\right] \tag{A.6}$$

Equation A.6 can be further simplified by multiplying the electric fields. The resultant expression is:

$$I_R = \left(A^2 - 2 \cdot A \cdot B \cdot \cos(\phi) + B^2\right) \cdot \left[\overrightarrow{E_{in_p}} \cdot \overrightarrow{E^*_{in_p}} - \overrightarrow{E_{in_p}} \cdot \overrightarrow{E^*_{in_s}} - \overrightarrow{E^*_{in_p}} \cdot \overrightarrow{E_{in_s}} + \overrightarrow{E_{in_s}} \cdot \overrightarrow{E^*_{in_s}}\right] \tag{A.7}$$

The terms $\overrightarrow{E_{in_p}} \cdot \overrightarrow{E^*_{in_s}}$ and $\overrightarrow{E^*_{in_p}} \cdot \overrightarrow{E_{in_s}}$ are equal to 0 because fields with different polarizations do not interact with each other. The terms $\overrightarrow{E_{in_p}} \cdot \overrightarrow{E^*_{in_p}}$ and $\overrightarrow{E_{in_s}} \cdot \overrightarrow{E^*_{in_s}}$ give, respectively, the irradiances I_{in_p} and I_{in_s}. Thus, the resulting equation obtained is:

$$I_R = \left(A^2 - 2 \cdot A \cdot B \cdot \cos(\phi) + B^2\right) \left[I_{in_p} + I_{in_s}\right] \tag{A.8}$$

The two irradiances can be summed and the sum is defined as I_i. The final expression is:

$$I_R = \left(A^2 - 2 \cdot A \cdot B \cdot \cos(\phi) + B^2\right) I_i \tag{A.9}$$

Appendix B

Derivation of the Irradiance of two Cascaded Fabry Perot interferometers

The electric field of two cascaded FP interferometers has the following form:

$$\overrightarrow{E_R} = \left(AA_1 - AB_1 e^{i\phi_1} - A_1 B e^{i\phi} + BB_1 e^{i(\phi_1+\phi)} \right) \overrightarrow{E_0} \tag{B.1}$$

The irradiance is given by:

$$I = \overrightarrow{E} \cdot \overrightarrow{E^*} \tag{B.2}$$

Substituting equation B.2 in equation B.1, it is obtained the following expression:

$$\begin{aligned} I_R = & \left[\left(AA_1 - AB_1 e^{i\phi_1} - A_1 B e^{i\phi} + BB_1 e^{i(\phi_1+\phi)} \right) \overrightarrow{E_0} \right] \cdot \\ & \left[\left(AA_1 - AB_1 e^{-i\phi_1} - A_1 B e^{-i\phi} + BB_1 e^{-i(\phi_1+\phi)} \right) \overrightarrow{E_0^*} \right] \end{aligned} \tag{B.3}$$

By multiplying the terms, it is obtained:

$$\begin{aligned} I_R = & \left(AA_1 - AB_1 e^{i\phi_1} - A_1 B e^{i\phi} + BB_1 e^{i(\phi_1+\phi)} \right) \cdot \\ & \left(AA_1 - AB_1 e^{-i\phi_1} - A_1 B e^{-i\phi} + BB_1 e^{-i(\phi_1+\phi)} \right) \\ & \overrightarrow{E_0} \cdot \overrightarrow{E_0^*} \end{aligned} \tag{B.4}$$

The equation is further simplified:

$$\begin{aligned}\frac{I_R}{I_0} &= A^2A_1^2 + A^2B_1^2 + A_1^2B^2 + B^2B_1^2 \\ &- A^2A_1B_1\left(e^{-i\phi_1} + e^{i\phi_1}\right) \\ &- AA_1^2B\left(e^{-i\phi} + e^{i\phi}\right) \\ &+ AA_1BB_1\left(e^{-i(\phi_1+\phi)} + e^{i(\phi_1+\phi)}\right) \\ &+ AA_1BB_1\left(e^{-i(\phi_1-\phi)} + e^{i(\phi_1-\phi)}\right) \\ &- ABB_1^2\left(e^{-i\phi} + e^{i\phi}\right) \\ &- A_1B^2B_1\left(e^{-i\phi_1} + e^{i\phi_1}\right)\end{aligned} \tag{B.5}$$

Since $e^{i\phi} + e^{-i\phi} = 2\cos(\phi)$, the equation B.5 is rewritten in the following form:

$$\begin{aligned}\frac{I_R}{I_0} &= A^2A_1^2 + A^2B_1^2 + A_1^2B^2 + B^2B_1^2 \\ &- 2A^2A_1B_1\cos\left(\phi_1\right) \\ &- 2AA_1^2B\cos\left(\phi\right) \\ &+ 2AA_1BB_1\cos\left(\phi_1+\phi\right) \\ &+ 2AA_1BB_1\cos\left(\phi_1-\phi\right) \\ &- 2ABB_1^2\cos\left(\phi\right) \\ &- 2A_1B^2B_1\cos\left(\phi_1\right)\end{aligned} \tag{B.6}$$

The final expression is:

$$\begin{aligned}\frac{I_R}{I_0} &= A^2A_1^2 + A^2B_1^2 + A_1^2B^2 + B^2B_1^2 \\ &+ 2AA_1BB_1\left[\cos\left(\phi_1+\phi\right) + \cos\left(\phi_1-\phi\right)\right] \\ &- 2\cos(\phi_1)\left(A^2A_1B_1 + A_1B^2B_1\right) \\ &- 2\cos(\phi)\left(AA_1^2B + ABB_1^2\right)\end{aligned} \tag{B.7}$$

Appendix C

Derivation of the Cross Correlation Signal

The signal in the time domain is given by:

$$I_R\left(t\right) \;=\; \int_{\beta_1}^{\beta_2} I_R(\beta)\, d\beta \tag{C.1}$$

where $I_R\left(\beta\right)$ is given by:

$$\begin{aligned} \frac{I_R}{I_0} &= C \\ &\quad - C_1 \cos\left(2\,\beta\, L\right) \\ &\quad - C_2 \cos\left(2\,\beta\, L_1\right) \\ &\quad + C_3 \left[\cos\left(2\,\beta\, L_1 + 2\,\beta\, L\right) + \cos\left(2\,\beta\, L_1 - 2\,\beta\, L\right)\right] \end{aligned} \tag{C.2}$$

where

$C = A^2A_1^2 + A^2B_1^2 + A_1^2B^2 + B^2B_1^2$,
$C_1 = 2\left(AA_1^2B + ABB_1^2\right)$,
$C_2 = 2\left(A^2A_1B_1 + A_1B^2B_1\right)$,
$C_3 = 2AA_1BB_1$

The integral is the sum of many integrals. All the integrals except the first one where it is just the integration of the constant C will be of the form:

$$\int_{\beta_1}^{\beta_2} \cos(A\beta)\, d\beta \tag{C.3}$$

where A is a generic constant. The solution of the integral from equation C.3 is of the form:

$$I = \frac{\sin(A\beta_2)}{A} - \frac{\sin(A\beta_1)}{A} \tag{C.4}$$

Multiplying and dividing the first and second terms on the right hand side of equation C.4 by β_2 and β_1 respectively the resulting equation is:

$$I = \beta_2 \frac{\sin(A\beta_2)}{A\beta_2} - \beta_1 \frac{\sin(A\beta_1)}{A\beta_1} \tag{C.5}$$

Since $sinc\,(x) = \frac{sin(x)}{x}$ equation C.5 is simplified:

$$I = \beta_2\, sinc\,(A\beta_2) - \beta_1\, sinc\,(A\beta_1) \tag{C.6}$$

This calculation can be done for all integrals in equation C.2 and the final expression has the following form:

$$\begin{aligned} I_{out}(t) &= C \cdot [\beta_2 - \beta_1] \\ &- C_1 \cdot \left[\beta_2 \cdot sinc\,(2\beta_2 L) - \beta_1 \cdot sinc\,(2\beta_1 L)\right] \\ &- C_2 \cdot \left[\beta_2 \cdot sinc\,(2\beta_2 L_1(t)) - \beta_1 \cdot sinc\,(2\beta_1 L_1(t))\right] \\ &+ C_3 \cdot \beta_2 \cdot \left[sinc\left[2\beta_2 (L_1(t) + L)\right] + sinc\left[2\beta_2 (L_1(t) - L)\right]\right] \\ &+ C_3 \cdot \beta_1 \cdot \left[sinc\left[2\beta_1 (L_1(t) + L)\right] + sinc\left[2\beta_1 (L_1(t) - L)\right]\right] \end{aligned} \tag{C.7}$$

Appendix D

Python Script

```
1
# Modules that allow the communication with the oscilloscope and data
    manipulation.
3 import App
import numpy as np
5 import pandas as pd

7 # A Function to establish communication with the oscilloscope and obtain the data
    .

9 def run(name='test.csv',save=0,showplot=0):
    cmd='COM'
11  port='COM'
    dso = App.dso2ke.Dso(port) # opens the port of the oscilloscope
13
    dso.chnum=4 # the number of channels
15
    for i in range(1,5):
17      dso.getRawData(True, i) # obtains the data of the four channels

19  # creates the time array from the scope data
    num=dso.points_num
21  dt=dso.dt[0]
    t_start=dso.hpos[0]-num*dt/2
23  t_end  =dso.hpos[0]+num*dt/2
```

```
    t = App.np.arange(t_start, t_end, dt)

    if((len(t)-num)==1): #Avoid floating point rounding error.
        t=t[:-1]

    # converts the binary data into values with base ten (what is seen on the
    oscilloscope)
    ch1 = dso.convertWaveform(0, 1)
    ch2 = dso.convertWaveform(1, 1)
    ch3 = dso.convertWaveform(2, 1)
    ch4 = dso.convertWaveform(3, 1)

    # makes the plot of the four channels
    App.plt.plot(t,ch1)
    App.plt.plot(t,ch2)
    App.plt.plot(t,ch3)
    App.plt.plot(t,ch4)


    # the data are stored in column format. Each column corresponds to the x and
    y values of the channels.

    ch1x = np.reshape(t, (len(t), 1), order='C')
    ch2x = np.reshape(t, (len(t), 1), order='C')
    ch3x = np.reshape(t, (len(t), 1), order='C')
    ch4x = np.reshape(t, (len(t), 1), order='C')

    ch1y = np.reshape(ch1, (len(ch1), 1), order='C')
    ch2y = np.reshape(ch2, (len(ch2), 1), order='C')
    ch3y = np.reshape(ch3, (len(ch3), 1), order='C')
    ch4y = np.reshape(ch4, (len(ch4), 1), order='C')

    df1 = np.append(ch1x, ch1y, axis=1)
    df2 = np.append(ch2x, ch2y, axis=1)
    df3 = np.append(ch3x, ch3y, axis=1)
    df4 = np.append(ch4x, ch4y, axis=1)

    df12 = np.append(df1, df2, axis=1)
```

```
    df34 = np.append(df3, df4, axis=1)
61
    df14 = np.append(df12, df34, axis=1)
63
    df14_2 = pd.DataFrame(data=df14)
65
    # stores the data in a CSV file
67  df14_2.to_csv(name, encoding='utf-8', index=False, sep=',')

69  if showplot:
        App.plt.show()
```

Appendix E

Calibration Curve of the PZT

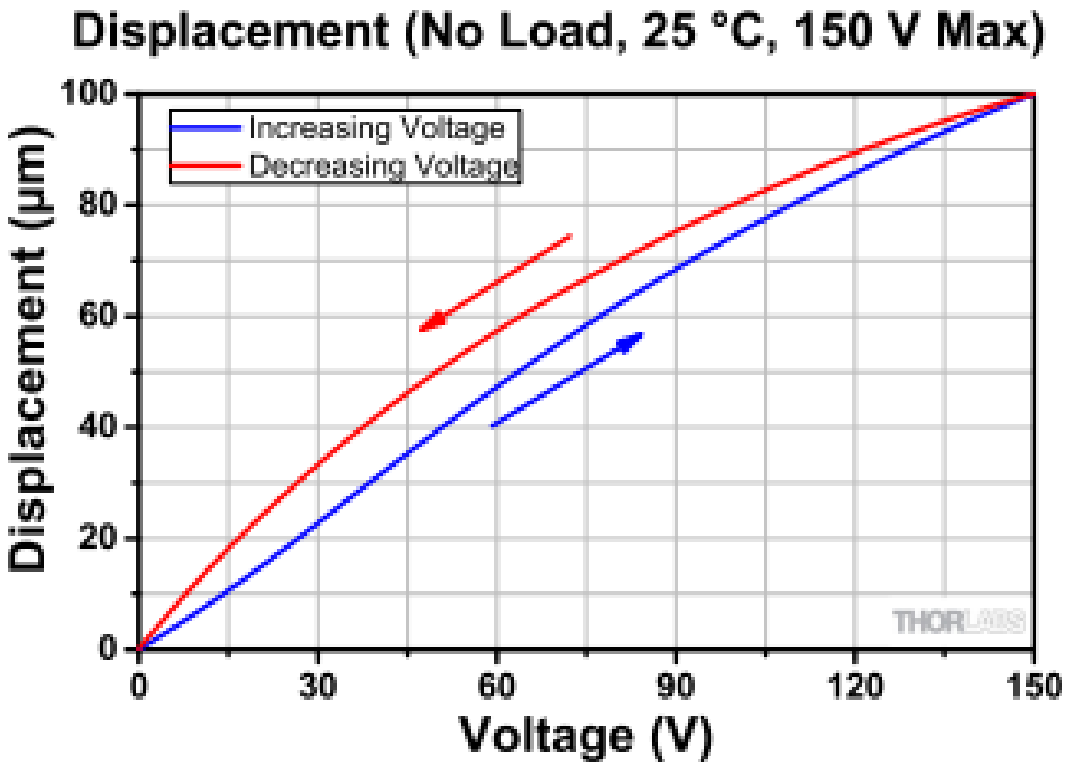

FIGURE E.1: Calibration Curve of the PZT adapted from ThorLabs

Bibliography

[1] E. Udd, "The emergence of fiber optic sensor technology," *Fiber Optic Sensors: An Introduction for Engineers and Scientists: Second Edition*, pp. 1–8, 7 2011.

[2] P. Roriz, L. Carvalho, O. Frazão, J. L. Santos, and J. A. Simões, "From conventional sensors to fibre optic sensors for strain and force measurements in biomechanics applications: A review," *Journal of Biomechanics*, vol. 47, pp. 1251–1261, 4 2014.

[3] P. Roriz, O. Frazão, A. B. Lobo-Ribeiro, J. L. Santos, and J. A. Simoes, "Review of fiber-optic pressure sensors for biomedical and biomechanical applications," *https://doi.org/10.1117/1.JBO.18.5.050903*, vol. 18, p. 050903, 5 2013.

[4] N. S. Kapany, "Fiber optics," *Scientific American*, vol. 203, pp. 72–81, 1960.

[5] N. Sabri, S. A. Aljunid, M. S. Salim, and S. Fouad, "Fiber optic sensors: Short review and applications," *Springer Series in Materials Science*, vol. 204, pp. 299–311, 2015.

[6] W. Lin, C. Zhang, L. Li, and S. Liang, "Review on development and applications of fiber-optic sensors," *2012 Symposium on Photonics and Optoelectronics, SOPO 2012*, 2012.

[7] M. R. Islam, M. M. Ali, M. H. Lai, K. S. Lim, and H. Ahmad, "Chronology of fabry-perot interferometer fiber-optic sensors and their applications: A review," *Sensors 2014, Vol. 14, Pages 7451-7488*, vol. 14, pp. 7451–7488, 4 2014.

[8] J. Mathew, O. Schneller, D. Polyzos, D. Havermann, R. M. Carter, W. N. MacPherson, D. P. Hand, and R. R. Maier, "In-fiber fabry-perot cavity sensor for high-temperature applications," *Journal of Lightwave Technology*, vol. 33, pp. 2419–2425, 6 2015.

[9] H. Sun, X. Zhang, L. Yuan, L. Zhou, X. Qiao, and M. Hu, "An optical fiber fabry-perot interferometer sensor for simultaneous measurement of relative humidity and temperature," *IEEE Sensors Journal*, vol. 15, pp. 2891–2897, 5 2015.

[10] B. Xu, D. N. Wang, J. Q. Li, and Y. M. Liu, "Fiber fabry–pérot interferometer for measurement of gas pressure and temperature," *Journal of Lightwave Technology, Vol. 34, Issue 21, pp. 4920-4925*, vol. 34, pp. 4920–4925, 11 2016.

[11] C. L. Lee, L. H. Lee, H. E. Hwang, and J. M. Hsu, "Highly sensitive air-gap fiber fabry-pérot interferometers based on polymer-filled hollow core fibers," *IEEE Photonics Technology Letters*, vol. 24, pp. 149–151, 2012.

[12] C. S. Monteiro, M. S. Ferreira, S. O. Silva, J. Kobelke, K. Schuster, J. Bierlich, and O. Frazão, "Fiber fabry-perot interferometer for curvature sensing," *Photonic Sensors 2016 6:4*, vol. 6, pp. 339–344, 10 2016.

[13] B. Xu, Y. Liu, D. Wang, D. Jia, and C. Jiang, "Optical fiber fabry-pérot interferometer based on an air cavity for gas pressure sensing," *IEEE Photonics Journal*, vol. 9, 4 2017.

[14] G. K. B. Costa, P. M. P. Gouvêa, L. M. B. Soares, J. M. B. Pereira, F. Favero, A. M. B. Braga, P. Palffy-Muhoray, A. C. Bruno, I. C. S. Carvalho, H. Aref, J. M. Baptista, J. L. Santos, H. Latifi, F. Farahi, J. Kobelke, K. Schuster, M. S. Ferreira, P. Roriz, J. Bierlich, K. Wondraczek, C. Aichele, O. Frazão, R. Zhao, X. g Huang, W. x He, and J. h Chen, "In-fiber fabry-perot interferometer for strain and magnetic field sensing," *Optics Express, Vol. 24, Issue 13, pp. 14690-14696*, vol. 24, pp. 14 690–14 696, 6 2016.

[15] J. M. López-Higuera, L. R. Cobo, A. Q. Incera, and A. Cobo, "Fiber optic sensors in structural health monitoring," *Journal of Lightwave Technology*, vol. 29, pp. 587–608, 2011.

[16] G. Wang, B. Liao, Y. Cao, X. Feng, B. O. Guan, and J. Yao, "Microwave photonic interrogation of a high-speed and high-resolution temperature sensor based on cascaded fiber-optic sagnac loops," *Journal of Lightwave Technology*, vol. 39, pp. 4041–4048, 6 2021.

[17] C. A. Díaz, C. Leitão, C. A. Marques, M. F. Domingues, N. Alberto, M. J. Pontes, A. Frizera, M. R. Ribeiro, P. S. André, and P. F. Antunes, "Low-cost interrogation technique for dynamic measurements with fbg-based devices," *Sensors 2017, Vol. 17, Page 2414*, vol. 17, p. 2414, 10 2017.

[18] J. Zheng, W. Li, and X. Liu, "Fast and simple interrogation of extrinsic fabry–perot interferometer sensor based on dual-wavelength intensity ratio," *Optics Communications*, vol. 439, pp. 176–180, 5 2019.

[19] K. Ogawa, S. Koyama, Y. Haseda, K. Fujita, H. Ishizawa, and K. Fujimoto, "Wireless, portable fiber bragg grating interrogation system employing optical edge filter," *Sensors 2019, Vol. 19, Page 3222*, vol. 19, p. 3222, 7 2019.

[20] C. Ma and A. Wang, "Signal processing of white-light interferometric low-finesse fiber-optic fabry perot sensors," *Applied Optics, Vol. 52, Issue 2, pp. 127-138*, vol. 52, pp. 127–138, 1 2013.

[21] R. M. Silva, A. Layeghi, M. I. Zibaii, H. Latifi, J. L. Santos, A. B. L. Ribeiro, and O. Frazao, "Interrogation sensing scheme based on a figure-of-eight fiber loop mirror," *IEEE Photonics Technology Letters*, vol. 25, pp. 745–748, 2013.

[22] J. Yi, "High-resolution interrogation technique for fiber optic extrinsic fabry-perot interferometric sensors by the peak-to-peak method," *Applied Optics*, vol. 47, pp. 925–932, 3 2008.

[23] W. R. Habel and K. Krebber, "Fiber-optic sensor applications in civil and geotechnical engineering," *Photonic Sensors 2011 1:3*, vol. 1, pp. 268–280, 3 2011.

[24] R. Correia, S. James, S. W. Lee, S. P. Morgan, and S. Korposh, "Biomedical application of optical fibre sensors," *Journal of Optics*, vol. 20, p. 073003, 6 2018.

[25] A. Dandridge and G. B. Cogdell, "Fiber optic sensors for navy applications," *IEEE LCS*, vol. 2, pp. 81–89, 1991.

[26] A. D. KERSEY, "Optical fiber sensors for permanent downwell monitoring applications in the oil and gas industry," *IEICE TRANSACTIONS on Electronics*, vol. E83-C, pp. 400–404, 3 2000.

[27] T. Yoshino, T. Ose, K. Kurosawa, and K. Itoh, "Fiber-optic fabry–perot interferometer and its sensor applications," *IEEE Transactions on Microwave Theory and Techniques*, vol. 30, pp. 1612–1621, 1982.

[28] A. D. Kersey, D. A. Jackson, and M. Corke, "A simple fibre fabry-pérot sensor," *Optics and Lasers in Engineering*, vol. 5, pp. 141–154, 1 1984.

[29] A. D. Kersey, D. D. Brennan, E. J. Friebele, J. S. Sirkis, M. A. Putman, and T. A. Berkoff, "In-line fiber étalon for strain measurement," *Optics Letters, Vol. 18, Issue 22, pp. 1973-1975*, vol. 18, pp. 1973–1975, 11 1993.

[30] E. Cibula and D. Donlagic, "All-fiber fabry-perot strain sensor," *https://doi.org/10.1117/12.566620*, vol. 5502, pp. 180–183, 6 2004.

[31] C. L. Lee, J. M. Hsu, J. S. Horng, and W. Y. Sung, "Microcavity fiber fabry-pérot interferometer with embedded golden thin film for high temperature measurement," *ISNE 2013 - IEEE International Symposium on Next-Generation Electronics 2013*, pp. 415–416, 2013.

[32] Y. Cui, Y. Jiang, T. Liu, J. Hu, and L. Jiang, "A dual-cavity fabry-perot interferometric fiber-optic sensor for the simultaneous measurement of high-temperature and high-gas-pressure," *IEEE Access*, vol. 8, pp. 80 582–80 587, 2020.

[33] Y. Jiang, "Fourier transform white-light interferometry for the measurement of fiber-optic extrinsic fabry-pérot interferometric sensors," *IEEE Photonics Technology Letters*, vol. 20, pp. 75–77, 1 2008.

[34] A. M. R. Pinto, J. Kobelke, J. L. Santos, K. Schuster, M. Lopez-Amo, and O. Frazão, "Interrogation of a suspended-core fabry–perot temperature sensor through a dual wavelength raman fiber laser," *Journal of Lightwave Technology, Vol. 28, Issue 21, pp. 3149-3155*, vol. 28, pp. 3149–3155, 11 2010.

[35] T. Saitoh, K. Nakamura, Y. Takahashi, and K. Miyagi, "Optical spectrum analyzer utilizing mems scanning mirror," *IEEE Photonics Technology Letters*, vol. 18, pp. 767–769, 3 2006.

[36] P. Kiesel, O. Schmidt, S. Mohta, N. Johnson, and S. Malzer, "Compact, low-cost, and high-resolution interrogation unit for optical sensors," *Applied Physics Letters*, vol. 89, p. 201113, 11 2006. [Online]. Available: https://aip.scitation.org/doi/abs/10.1063/1.2390650

[37] Q. Liu and W. Peng, "Fast interrogation of dynamic low-finesse fabry-perot interferometers: A review," *Microwave and Optical Technology Letters*, vol. 63, pp. 2279–2291, 9 2021.

[38] E. Udd, "An overview of fiber-optic sensors," *Review of Scientific Instruments*, vol. 66, p. 4015, 6 1998.

[39] K. Fidanboylu, "Fiber optic sensors and their applications," *undefined*, 2009.

[40] B. Gholamzadeh and H. Nabovati, "Fiber optic sensors," *International Journal of Electronics and Communication Engineering*, vol. 2, pp. 1107–1117, 6 2008.

[41] A. D. Kersey, "A review of recent developments in fiber optic sensor technology," *Optical Fiber Technology*, vol. 2, pp. 291–317, 7 1996.

[42] B. Culshaw and A. Kersey, "Fiber-optic sensing: A historical perspective," *Journal of Lightwave Technology*, vol. 26, pp. 1064–1078, 5 2008.

[43] F. L. Pedrotti and L. S. Pedrotti, *Introduction to Optics 2nd Edition*, 1993.

[44] M. Born, E. Wolf, A. B. Bhatia, P. C. Clemmow, D. Gabor, A. R. Stokes, A. M. Taylor, P. A. Wayman, and W. L. Wilcock, *Principles of Optics: Electromagnetic Theory of Propagation, Interference and Diffraction of Light*. Cambridge University Press, 10 1999.

[45] A. Lobo Ribeiro, "Esquemas de multiplexagem de sensores de fibra Óptica," Ph.D. dissertation, 10 1996.

[46] R. Hibbeler, *Mechanics of Materials*, 8th ed., P. Hall, Ed. Prentice Hall, 4 2010.

[47] S. Novais, M. S. Ferreira, and J. L. Pinto, "Fabry-perot cavity based on air bubble for high sensitivity lateral load and strain measurements," *https://doi.org/10.1117/12.2276342*, vol. 10453, pp. 698–702, 8 2017.

[48] S. J. Ling, J. Sanny, and W. Moebs, *University physics. Volume 2*, 2016.

[49] P. Roriz, S. Silva, O. Frazão, and S. Novais, "Optical fiber temperature sensors and their biomedical applications," *Sensors (Basel, Switzerland)*, vol. 20, 4 2020.

[50] H. Ito, T. Nagatsuma, and T. Ishibashi, "Uni-traveling-carrier photodiodes for high-speed detection and broadband sensing," *https://doi.org/10.1117/12.698221*, vol. 6479, pp. 150–163, 2 2007.